CHAPTER 5

SENSORLESS CONTROLLER DESIGN FOR THE NINE-PHASE IPM

designed based on the main component of the machine circuit. After modelling the nine phase converter the controller is designed using the minimum copper loss strategy. The current regulators are also designed using the regular dynamic equations of the machine in the rotor reference frame. To implement the precise control to the machine the rotor position is needed, therefore the position estimation met(rglet n)--c0912 frequency voltage is injected to a non

-torque producing channel of the machine and the position of the rotor is extracted from the high frequency currents due to the high frequency voltages. The general form of the high frequency currents is obtained using the harmonic balance technique and the essential signal processing method is presented to extract the position data from the currents. The presentation of the new position estimation method based on the high frequency voltage injection in the non-torque producing channel of the machine in stationary reference frame is the novel part of this chapter. The controller is simulated and tested using the full order model of the machine that was generated in the chapter 3. After confirming the performance of the controller and estimator with MATLAB simulation the controller and estimator are discretized and translated to C++ language to be implemented in DSP. Finally, the performance of the method is verified with experimental results. The steady state analyses of the machine are also presented in this

$$
\begin{aligned}
S_{ap} \quad S_{an} \quad 1 \\
S_{bp} \quad S_{bn} \quad 1 \\
S_{cp} \quad S_{cn} \quad 1 \\
S_{dp} \quad S_{dn} \quad 1 \\
S_{ep} \quad S_{en} \quad 1 \\
S_{fp} \quad S_{fn} \quad 1 \\
S_{gp} \quad S_{gn} \quad 1 \\
S_{hp} \quad S_{hn} \quad 1 \\
S_{ip} \quad S_{in} \quad 1
\end{aligned}
\tag{5.1}
$$

: K H U H S_{xp} ¶ µ D6 Q S_{xn} ¶ µ D6 U H W K H V Z L W F K L Q J I X Q F W L R Q V R I W K H W

µ [¶ R I W K H L Q Y H U W H U $ Q V R R X W S X W voltages of the inverter can be expressed as:

$$
\begin{aligned}
V_{AO} \quad \frac{V_{dc}}{2}(S_{ap} \quad S_{an}) \quad V_{DO} \quad \frac{V_{dc}}{2}(S_{dp} \quad S_{dn}) \quad V_{GO} \quad \frac{V_{dc}}{2}(S_{gp} \quad S_{gn}) \\
V_{BO} \quad \frac{V_{dc}}{2}(S_{bp} \quad S_{bn}) \quad V_{EO} \quad \frac{V_{dc}}{2}(S_{ep} \quad S_{en}) \quad V_{HO} \quad \frac{V_{dc}}{2}(S_{hp} \quad S_{hn}), \\
V_{CO} \quad \frac{V_{dc}}{2}(S_{cp} \quad S_{cn}) \quad V_{FO} \quad \frac{V_{dc}}{2}(S_{fp} \quad S_{fn}) \quad V_{IO} \quad \frac{V_{dc}}{2}(S_{ip} \quad S_{in})
\end{aligned}
\tag{5.2}
$$

$V_{dc} \quad 200V$

Using equation (5.1), the voltage equations can be rewritten as:

—

— (5.3)

—

: K H U H W K H V Z L W F K L Q J I X Q F W L R Q S_{xp} R ¶ µ and the expression W R S V Z L W F K

for the modulation index can be written as:

$$
\begin{aligned}
& \frac{a.4}{2} \\
B_n \quad & d_c \frac{b}{2} \\
C_n \quad & d_c \frac{c}{2} \\
D_n \quad & d_c \frac{d}{2} \\
E_n \quad & d_c \frac{e}{2} \\
F_n \quad & d_c \frac{f}{2} \\
G_n \quad & d_c \frac{g}{2} \\
H_n \quad & d_c \frac{h}{2} \\
I_n \quad & d_c \frac{i}{2}
\end{aligned}
\tag{5.6}
$$

Since the machine is controlled in the rotor reference frame the inverter, voltages also should be transformed to the rotor reference frame.

(5.7)

Equation (5.7) can be represented as equation (5.8).

a o a o
« » « »
« » « »
« » « »
« » « »
« » « »
« » « »
« » « »
« » « »
« » « »
« » « »
« » « »
« » « »
« » « »
¬ ¼ ¬ o ½
¼ 9 »

(5.8)

–

(5.9)

The stator copper loss can be defined as:

$$P_{loss} \quad \frac{9}{4} r_s \, i_{d1r}{}^{2} \quad i_{q1r}{}^{2} \tag{5.13}$$

$$(i_{d1r}, i_{q1r})_{center} = \left(\frac{\lambda_{pmd1r}}{2(L_{q1q1} - L_{d1d1})}, 0\right) \tag{5.23}$$

7KH HTXDWLRQ FRXOG EH FRQVLGHUHG DV D TXDG

Figure 5.3: The speed controller loop.

Substituting the electromagnetic torque to the equation (5.26) results in:

$$L_{q1q1} \quad L_{d1d1}{}^{2} i_{q1r}{}^{4} \quad \frac{4}{9P} \quad G_{z} \quad T_{L} \quad Q_{pmd1r} I_{q1r} \quad \frac{\S 4}{\copyright 9P} \quad G_{z} \quad T_{L} \quad \frac{\cdot^{2}}{\imath_{1}} \quad 0 \tag{5.29}$$

The PI controller for the speed controller loop can be designed using the mechanical dynamic equation as:

$$p Z_{r} \quad \frac{\S}{\copyright} K_{p Z} \quad \frac{K_{i Z}}{S} \cdot \frac{\cdot}{\imath_{1}} Z_{r}^{*} \quad Z_{r} \tag{5.30}$$

The above equation results in:

$$\frac{Z_{r}}{K_{r}^{Z}} \quad \frac{p Z \quad i Z}{p Z \quad K_{i Z}} \tag{5.31}$$

By setting the denominator of the transfer function to be equal to the second order Butterworth polynomial the controller coefficients can be designed [161].

$$S^{2} \quad K_{p Z} S \quad K_{i Z} \quad p^{2} \quad \sqrt{2} p Z_{o} \quad Z_{o} \tag{5.32}$$

The speed controller loop has to be at least 10 times faster than the desired rotor speed profile [157]. The final desired speed profile is a trapezoidal waveform that has the frequency of up to 0.05 (Hz). Therefore, the frequency of the speed controller loop has to be selected bigger than 0.5 (Hz). Setting $\tilde{n}_{\hat{a}} \; L \; y$ the correspondent relationship between the denominator of the transfer function and the Butterworth polynomial yields:

$$K_{p Z} \quad \sqrt{2} Z_{o} \quad 7\sqrt{2} \tag{5.33}$$

5.2.4 Current Regulator Design

Using the dynamic equations of the q and d axis voltages in the rotor reference frame, the current regulators for controlling the μ ¶and $\dot{\mu}_{d1r}$ ¶can be designed. The equations are repeated here from chapter 3.

r (5.35)

(5.36)

$$\frac{K_{iq}}{L_{q1q1}} \quad Z_o^2 \quad o \quad K_{iq} \quad 104 \tag{5.45}$$

The d axis current controller also can be designed as:

$$r_s i_{d1r} \quad pL_{d1d1} i_{d1r} \quad G_{ds} \quad K_{ds} \, i^*_{d1r} \quad i_{d1r} \tag{5.46}$$

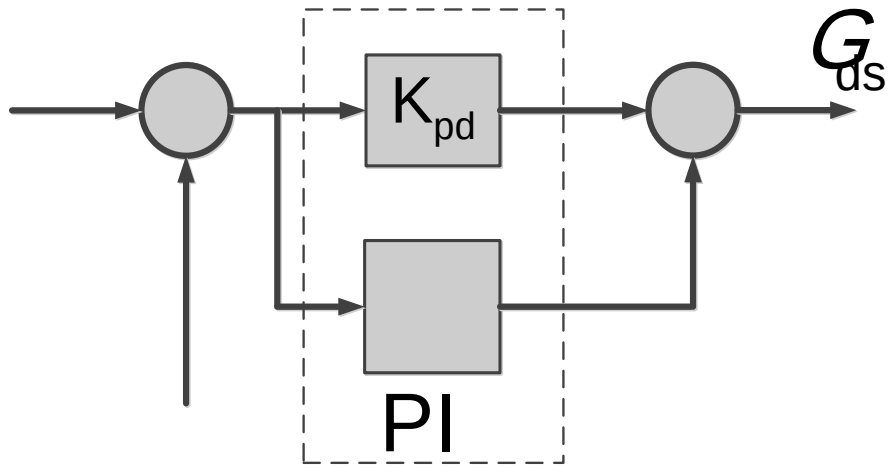

Figure 5.5: The d axis current regulator.

According to the Figure 5.5 the - × æ can be considered as a PI controller according to equation (5.47).

$$K_{ds} \quad \left(K_{pd} \quad \frac{K_{id}}{S} \right) \tag{5.47}$$

$$r_s i_{d1r} \quad pL_{d1d1} i_{d1r} \quad G_{ds} \quad \left(K_{pd} \quad \frac{K_{id}}{S} \right) i^*_{d1r} \quad i_{d1r} \tag{5.48}$$

$$r_s i_{d1r} \quad pL_{d1d1} i_{d1r} \quad K_{pd} i_{d1r} \quad \frac{K_{id}}{S} i_{d1r} \quad \left(K_{pd} \quad \frac{K_{id}}{S} \right) i^*_{d1r} \tag{5.49}$$

$$\frac{i_{d1r}}{i^{*}_{d1r}} \quad \frac{\left(K_{pd} \quad \frac{K_{id}}{S}\right)}{r_s \quad pL_{d1d1} \quad K_{pd} \quad \frac{K_{id}}{S}} \quad \frac{\left(pK_{pd} \quad \frac{K_{id}}{L_{d1d1}}\right)}{p^2 \quad p\frac{r_s \quad K_{pd}}{L_{d1d1}} \quad \frac{K_{id}}{L_{d1d1}}} \tag{5.50}$$

The denominator of the equation (5.50) can be set equal to the second order Butterworth polynomial to obtain the K_{pd} and K_{id}.

$$\sqrt{2} \quad \frac{\quad pd}{\quad d1d1} \tag{5.51}$$

By substituting the L_{d1d1}=0.0012 (H), the controller coefficients can be calculated as:

$$K_{pd} \quad \sqrt{2}\,\omega_o L_{d1d1} \quad r_s \quad \sqrt{2} \times 200 \times 0.0012 \quad 0.01 \quad 0.3294 \tag{5.52}$$

measurement and the flux linkages (λ_{q1r} D Q λ_{d1r}) are calculated using the stator inductances and feedback currents. Since the load torque is not known the T_L is set equal to zero which means the load torque will be the system disturbance. In this procedure the exact position of the rotor flux linkage ($\dot{\xi}_r$) is needed. The goal of the next sections of this chapter is to design an estimator to

) are proc

$$g^{-1}(\theta,\tau_f) = a_0 + a_1\cos 2(\theta - \tau_f) + a_2\cos 6(\theta - \tau_f)$$

$$a_3\cos 10(\theta - \tau_f) + a_4\cos 14(\theta - \tau_f) \tag{5.58}$$

$$a_0 = a,\ a_1 = b,\ a_2 = \frac{b}{3},\ a_3 = \frac{b}{5},\ a_4 = \frac{b}{7}$$

$$a = \frac{1}{2}\left(\frac{1}{g_b} - \frac{1}{g_b}\right);\quad b = \frac{1}{2}\left(\frac{1}{g_b} - \frac{1}{g_a}\right);$$

Using the Fourier series of the winding function, the air gap function and also the equation (3.4) the self and mutual inductances can be expressed as equation (5.59) [87].

$$L_{jk} = 2\mu_o rl[a_o(N_1^2\cos(k-j)\Delta + \frac{N_7^2}{49}\cos 7(k-j)\Delta + \frac{N_5^2}{25}\cos 5(k-j)\Delta$$

$$\frac{N_3^2}{9}\cos 3(k-j)\Delta + \frac{1}{2}(a_1N_1^2)\cos(2(k-j)\Delta - 2\tau_f)$$ (5.59)

$$\frac{1}{2}(\frac{a_2N_3^2}{9})\cos(6k(k-j)\Delta - 6\tau_f) + \frac{1}{2}(\frac{a_3N_5^2}{25})\cos(10k(k-j)\Delta$$

$$10\tau_f) + (\frac{a_4N_7^2}{98})\cos(14k(k-j)\Delta - 14\tau_f)],\quad \Delta = \frac{2\pi}{9}$$

:KHUH ³N´ DQG µM¶ UHSUHVHQW WKH SDLUV RI VWDWRU SRVH Q according to Table 5.1, a_i are the coefficients of the Fourier VHULHV RI WKH DLU JDS IXQFWLRQ N_i´SUHVHQW represents the coefficients of the Fourier series of the winding functions. For example, the self-LQGXFWDQFHV RI WKH SKDVH Q can be expressed as equation (5.60). FD

(5.62)

$$\begin{bmatrix} v_{q3} \\ v_{d3} \end{bmatrix} = \begin{bmatrix} \cos(\omega_s t) \\ \cos(\omega_s t - \frac{\pi}{2}) \end{bmatrix} r_s \begin{bmatrix} i_{q3} \\ i_{d3} \end{bmatrix} + p \begin{bmatrix} \lambda_{q3} \\ \lambda_{d3} \end{bmatrix} \tag{5.69}$$

The $q_3 d_3$ flux linkage equations are:

$$\begin{bmatrix} \lambda_{q3} \\ \lambda_{d3} \end{bmatrix} = \begin{bmatrix} L_{q3} & 0 \\ 0 & L_{d3} \end{bmatrix} \begin{bmatrix} i_{q3} \\ i_{d3} \end{bmatrix} \tag{5.70}$$

The equations (5.69) and (5.70) result in:

—

Figure 5.7: The rotor of the machine.

The dynamic equations of the rotor are presented in equation (5.91). Using that, the observer can be designed as equation (5.92) which is the standard form of a close loop observer [160]. In

W K L V H T X D W L R Q µ $ ¶ U H S U H V H Q W V W K H V \ V W H P P D W U L [µ %

µ & ¶ L V W K H R X W S X W P D W U L [D Q G µ ; ¶ U H S U H V H Q W V W K H V W

(5.91)

CX

$$\ddot{X} \quad A\ddot{X} \quad BU \quad K(Y \quad C\ddot{X}) \tag{5.92}$$

In the equation (5.92) the term á is the estimated state variables. The error between the estimated and real state and also the derivation of the error are:

$$e \quad X \quad \dot{X} \tag{5.93}$$

$$e \quad X \quad \dot{X} \tag{5.94}$$

Substituting the : 6 and : à 6 from equations (5. 93) and (5.94) in to the (5.92) results in:

$$e \quad AX \quad BU \quad A\ddot{X} \quad BU \quad K(CX \quad C\ddot{X}) \tag{5.95}$$

Rearranging the equation results in:

$$e \quad A\,X \quad \ddot{X} \quad K(CX \quad C\ddot{X}) \quad Ae \quad KCe \tag{5.96}$$

The standard form of mechanical dynamic equations can be written as:

$$p\begin{bmatrix}\omega_r \\ \theta_r\end{bmatrix} = \begin{bmatrix}-\frac{PB}{2J} & 0 \\ 1 & 0\end{bmatrix}\begin{bmatrix}\omega_r \\ \theta_r\end{bmatrix} + \begin{bmatrix}\frac{P}{2J} \\ 0\end{bmatrix}T_e + \begin{bmatrix}-\frac{P}{2J} \\ 0\end{bmatrix}T_L \tag{5.97}$$

The observer is a closed loop one. According to the equation (5.88) the input signals carry the information of the position, therefore to be able to compare the output and the input, the output of the system has to be the position. Based on that the output is defined as:

$$Y = \begin{bmatrix}0 & 1\end{bmatrix}\begin{bmatrix}\omega_r \\ \theta_r\end{bmatrix} \tag{5.98}$$

Substituting the mechanical dynamic equations to the observer equations results in:

$$p\hat{\omega}_r = -\frac{PB}{2J}\hat{\omega}_r + K_1\left(\theta_r - \hat{\theta}_r\right) + \frac{P}{2J}T_e - T_L \tag{5.99}$$

$$p\hat{\theta}_r = \hat{\omega}_r + K_2\left(\theta_r - \hat{\theta}_r\right) \tag{5.100}$$

Using the equations (5.99) and (5.100), the position estimator can be built according to Figure 5.8.

To design the observer gains (K_1, K_2) the characteristic polynomial of the observer is needed. The characteristic polynomial of the observer can be derived using the procedure outlined below.

The errors can be defined as:

$$e_1 = \omega_r - \hat{\omega}_r \tag{5.101}$$

$$e_2 = \theta_r - \hat{\theta}_r \tag{5.102}$$

Therefore, the derivative of the rotor speed error can be shown as:

(5.108)

By defining a new state variable as equation (5.109) the state space equations of the observer can be represented as equation (5.110).

$$pe_3 \quad e_2 \tag{5.109}$$

$$\begin{aligned} \quad & \quad \quad \quad

$$\omega_n \approx \omega_{r\,Ratted} \approx \omega_o \tag{5.114}$$

8VLQJ WKH HTXDWLRQ VHOHFWHG ZKHQ ω_n LV VHW WR (Rad/Sec). Therefore, using the equation (5.113) the coefficients of the observer can be designed as:

$$\begin{aligned} \lambda &= \left(\frac{K_{p2}}{\omega_n^2} - \frac{PB}{2J}\right) \\ \mu &= \left(\frac{PBK_{p2}}{2J} - K_{p1}\right) - K_{I1} \end{aligned} \tag{5.115}$$

$$\lambda = 1000 \qquad \mu = 500000 \qquad \nu = 125000000$$

(a)

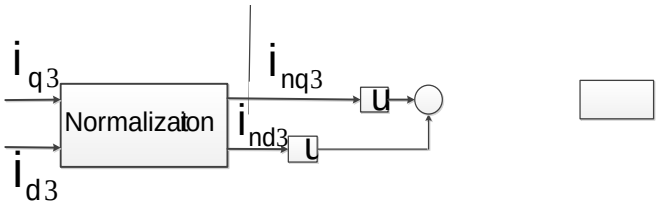

(b)

Figure 5.9: (a) The block diagram used to extract signal for observer, (b) The Luenberger observer.

Substituting machine parameters from Table 5.2 in to the equation (5.115), the different coefficients of the observer can be calculated as:

$$\lambda = \frac{K_{p2}}{\omega_n^2} = 1000 \qquad \nu = \frac{K_{p2}}{\omega_n^2} = 999.9 \tag{5.116}$$

$$\mu = \left(\frac{PBK_{p2}}{2J} - K_{p1}\right) - K_{I1} = 500000 \qquad \nu = K_{p1} = 499900.1 \tag{5.117}$$

$$K_{I1} \quad 125000000 \tag{5.118}$$

7 K H L Q S X W R I W K H Z K L O H W K H L R V H U Y H U L V I H G Z L W K V high frequency signal injection. The input signals which are derived in the section 5.2 have the form of the equation (5.88) by separating the real and imaginary parts of the signal they can be shown as equations (5.119) and (5.120) respectively.

$$i_{nq3} \quad \mathrm{Sin}(6\ T_f) \tag{5.119}$$

$$i_{nd3} \quad \mathrm{Cos}(6\ T_f)$$

magnitude to bring the magnitude to unity. The second part is heterodyning to compare the input position with the estimated one and calculate the error between the input angle and the estimated angle. The third part is the PI controller of the observer to force the observer to operate at zero error in steady state. And the last part is the mechanical model of the rotor to calculate the rotor speed and the rotor position.

5.4.2 Design of the Low Pass Filters

According to the Figure 5.9 the observer also has a low pass filter which removes the extra high frequency components of the signals after the heterodyning process. The low pass filter general form is presented in equation (5.124).

$$f \quad \frac{Z_n^2}{S^2 \quad 2\,\zeta_n S \quad Z_n^2}$$

5.4.3 Robustness of the Observer

$$\left| \qquad \right|$$

$$\frac{{}_{3} \qquad {}_{3}}{{}_{3} \quad {}_{3}\sin(3 \quad)} \qquad \frac{{}_{3}\cos(6 \quad) \; 6 \qquad {}_{3}\cos(6 \quad)}{0.5 \quad {}_{3} \quad {}_{3}\sin(3 \quad)}$$

$$^{2} \qquad \frac{{}_{3}\sin(6 \quad) \; 6 \qquad {}_{3}\sin(6 \quad) \qquad {}_{3}\cos(6 \quad) \; 6 \qquad {}_{3}\cos(6 \quad)}{0.5 \quad {}_{3} \quad {}_{3}\sin(3 \quad)}$$

$$\frac{{}_{3}\sin(6 \quad) \; 6 \qquad {}_{3}\sin(6 \quad) \qquad {}_{3}\cos(6 \quad) \; 6 \qquad {}_{3}\cos(6 \quad)}{0.5 \quad {}_{3} \quad {}_{3}\sin(3 \quad)^{2}}$$

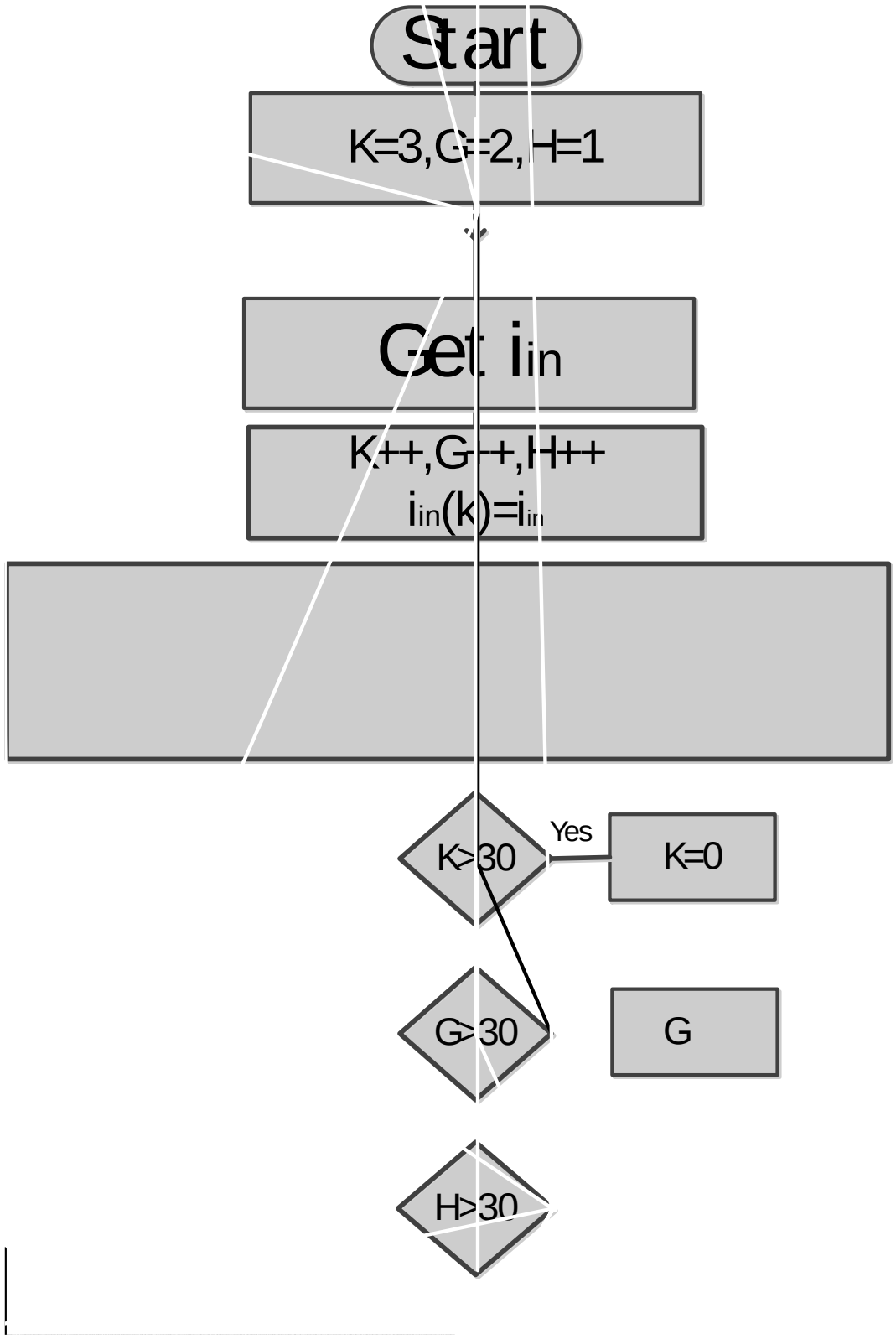

Figure 5.13: The flow chart for the filter.

$$\frac{\ddot{\theta}_r}{H} \quad \frac{K_{I1}T\,1 \quad z^{1\ 3} \quad 2K_{p1}\,1 \quad z^{1}\ T\,1 \quad z^{1\ 2} \quad JK_{p2}\,2\,1 \quad z^{1\ 2}\,T\,1 \quad z^{1}}{2J\,1 \quad z^{1\ 3}} \tag{5.159}$$

And from there:

$$\begin{aligned} &2J\,\ddot{\theta}_r \quad 2J\,\ddot{\theta}_r \quad 3z^{1} \quad 3z^{2} \quad z^{3} \quad K_{I1}T^{3}\,1 \quad 3z^{1} \quad 3z^{2} \quad z^{3} \\ &2K_{p1}T^{2}\,1 \quad z^{1} \quad z^{2} \quad z^{3} \quad 4TJK_{p2}\,1 \quad z^{1} \quad z^{2} \quad z^{3} \end{aligned} \tag{5.160}$$

$$\begin{aligned} &2 \quad \ddot{O} \quad 6 \quad \ddot{O} \quad 1 \quad 6 \quad \ddot{O} \quad 2 \quad 2 \quad \ddot{O} \quad 3 \quad {}_{1}^{3} \\ &3 \quad {}_{1}^{3} \quad 1 \quad 3 \quad {}_{1}^{3} \quad 2 \quad {}_{1}^{3} \quad 3 \quad 2 \quad {}_{1}^{2} \\ &2 \quad {}_{1}^{2} \quad 1 \quad 2 \quad {}_{1}^{2} \quad 2 \quad 2 \quad {}_{1}^{2} \quad 3 \quad 4 \quad {}_{2} \\ &4 \quad {}_{2} \quad 1 \quad 4 \quad {}_{2} \quad 2 \quad 4 \quad {}_{2} \quad 3 \end{aligned} \tag{5.161}$$

Where:

(5.162)

Using the Equation (5.162) the flow chart of the observer can be presented as Figure 5.15.

5.6 Sensorless Nine-Phase IPM Drive

In this section, the performance of the designed position observer and the controller are verified using simulation and experimental results. The simulation is done using MATLAB/Simulink and the experiment is done using DSP-FPGA controller.

5.6.1 Constant Volt/Hz Open-

addition to the fundamental voltage under a constant Volt/Hz (V/f 1.8) open-loop operation. The high frequency voltage (980Hz), (5V peak) set is injected in the third sequence channel of the machine. In simulation the initial speed of the machine is set at the negative rated and it increases to zero and after a short stop, the speed increases to the positive rated speed. Similarly, the proposed rotor angle estimation method has been implemented on a 2hp, nine-phase IPM using a DSP-FPGA controller which controls the machine via a nine phase voltage source inverter (switching frequency of 6 kHz).

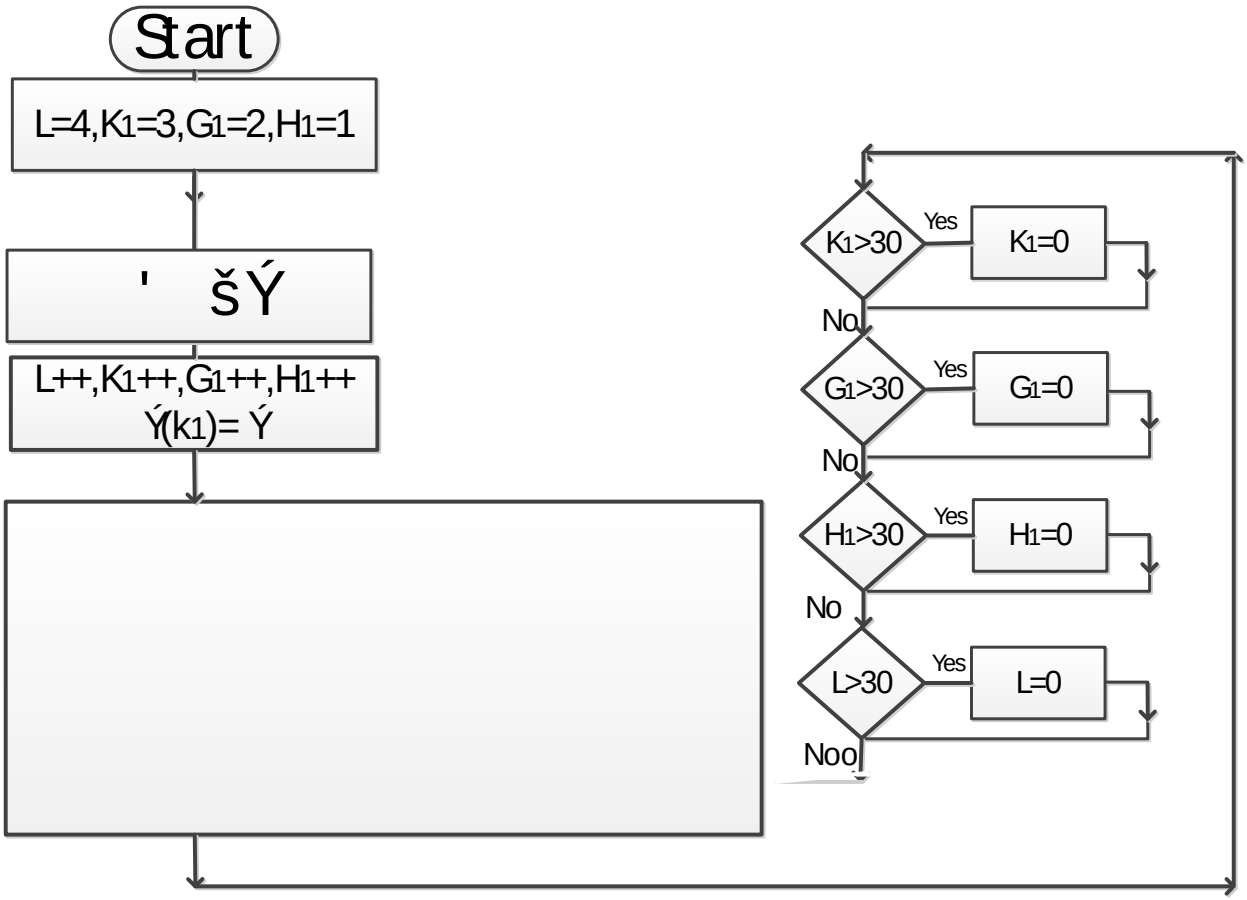

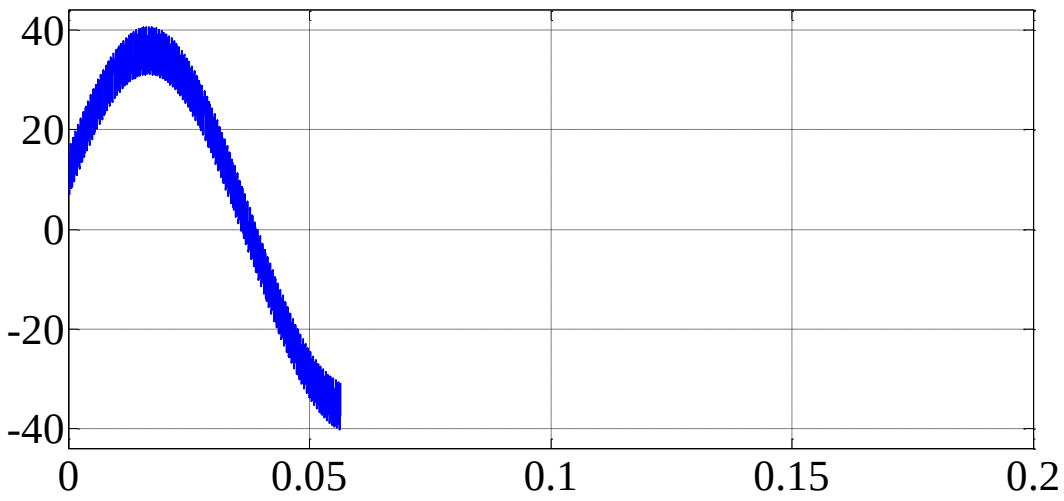

Figure 5.16: Simulation results for the nine-phase voltages applied to the stator windings.

The discretized model of the observer has been implemented in the DSP (DSK TMS320C6713). The current sensors are connected to the controller with nine Analog/Digital converters with the sampling rate of 50 kHz. After generating the high frequency voltages inside the DSP they are sent to the FPGA which generates the PWM pulses for the inverter. Figure 5.16 and 5.17 show stator voltages after high frequency injection for simulation and experimental results respectively.

(5.163)

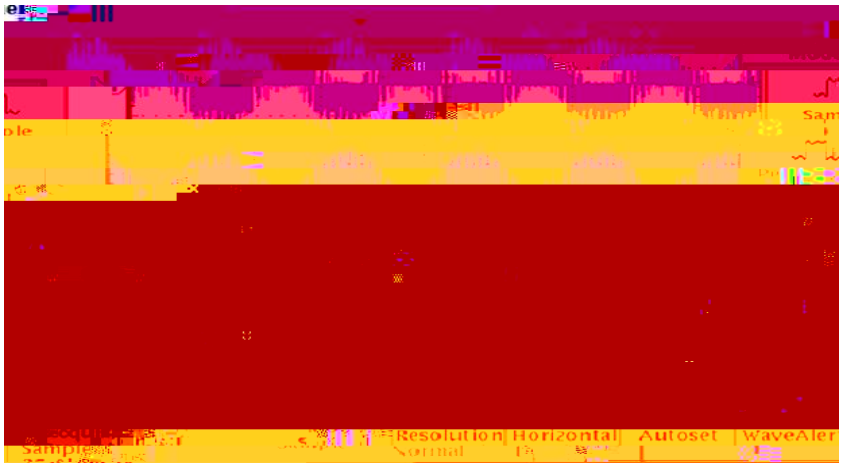

(a)

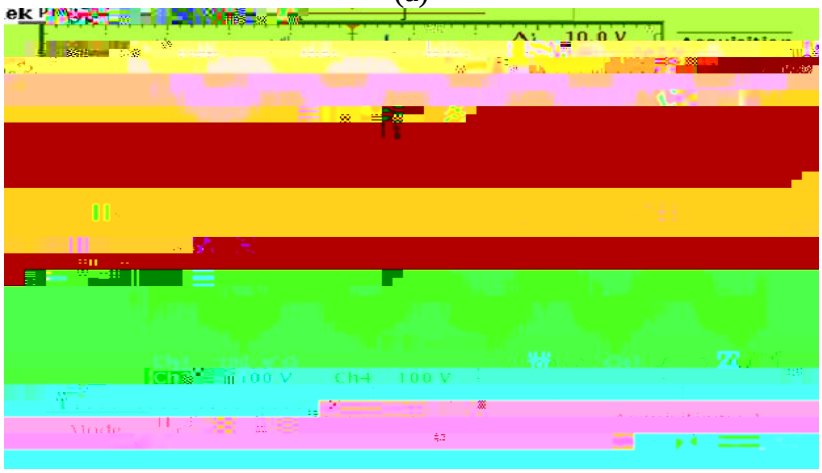

(b)

(c)

Figure 5.17: Experimental results for the nine-phase voltages applied to the stator windings,

D 3 K D V H V µ D ¶ µ G ¶ D Q G µ J ¶ E 3 K D V H V (4 µ E ¶ µ H ¶ Volt/scale).

Nine-phase currents of the machine for simulation and experimental results are shown in Figures 5.18 and 5.19 respectively. From these figures, the effect of the stator magnetic saturation

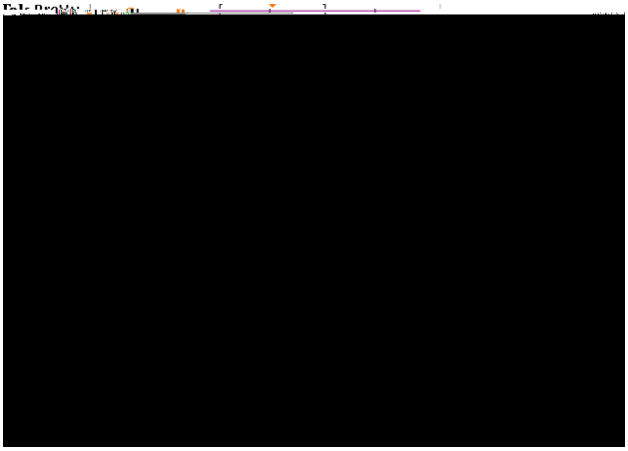

(a)

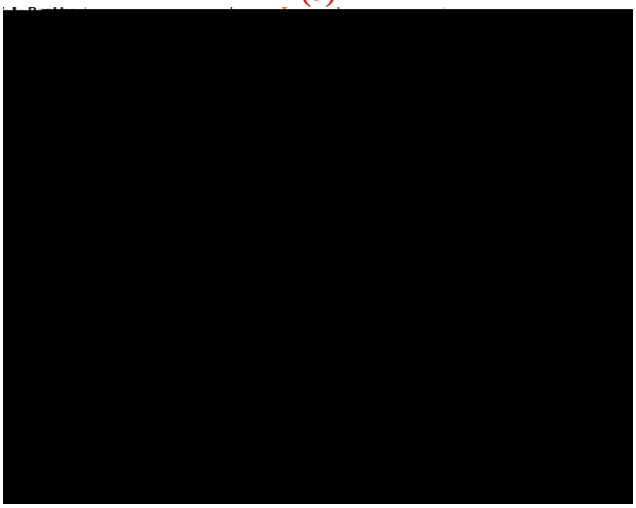

(b)

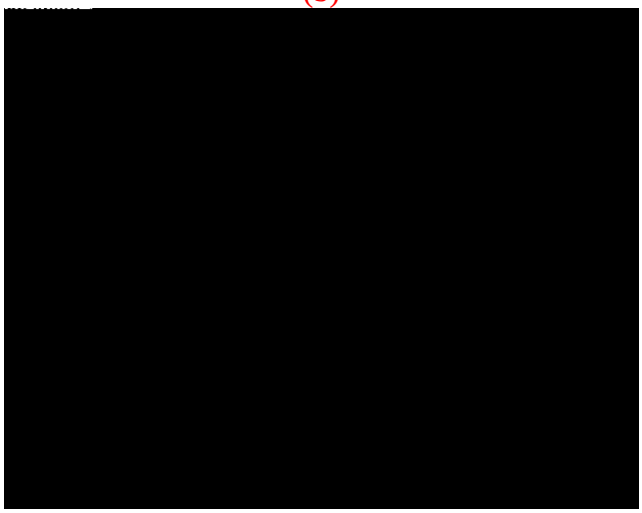

(c)

Figure 5.19: Experimental results for the nine

It is noted that since the high frequency currents are extracted using the sequence analysis in the stationary reference frame, there is no need for heterodyning and high pass filtering of the

high frequency parts and also they are normalized to have unity magnitude to be compatible with the observer.

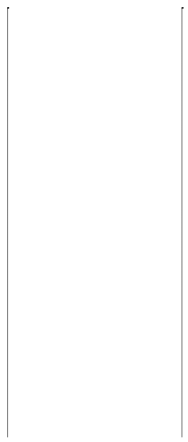

Figure 5.28: The third sequence of the current in stationary reference frame (i_{q3}, i_{d3}) after heterodyning and filtering (simulation results).

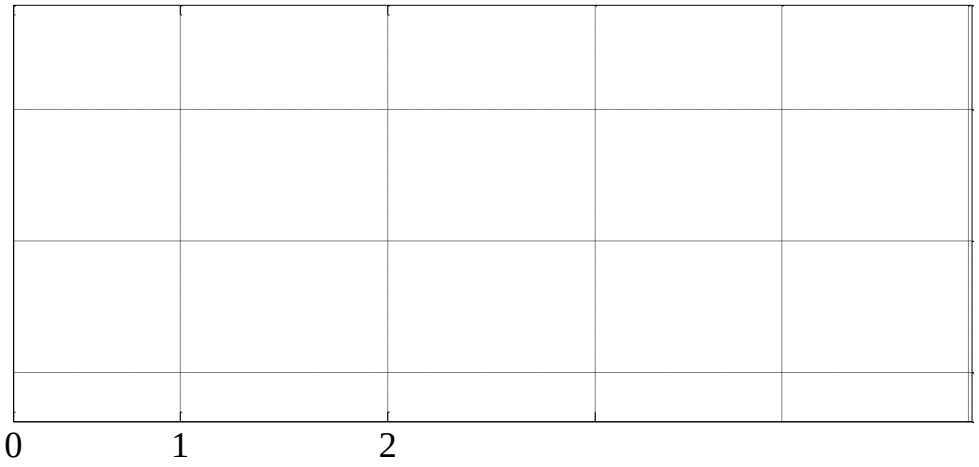

Figure 5.29: The third sequence of the current in stationary reference frame (i_{q3}, i_{d3}) after heterodyning and filtering (experimental results).

The resulting currents after, filtering and normalizing, are shown in the Figure 5.30 and 5.31 for simulation and experimental results, respectively.

Figure 5.30: The third sequence of the current in stationary reference frame (i_{qn3}, i_{dn3}) after normalizing (simulation results).

Figure 5.31: The third sequence of the current in stationary reference frame (i_{qn3}, i_{dn3}) after normalizing (experimental results).

In the third harmonic currents, the measured currents show more ripples than the simulated ones. The ripples are mostly coming from sampling noise of the prototype.

the negative, positive and also zero rotor speed regions the rotor position observer follows the rotor position precisely.

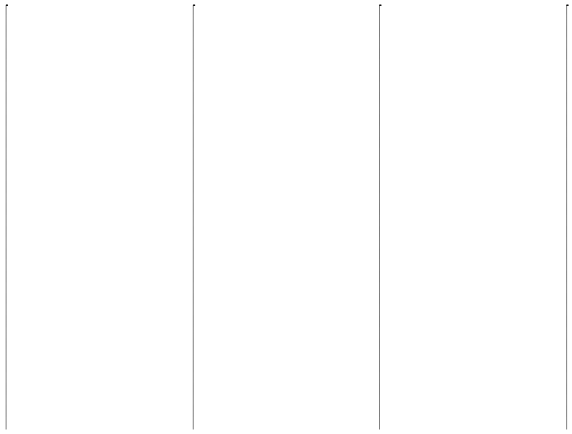

(a)

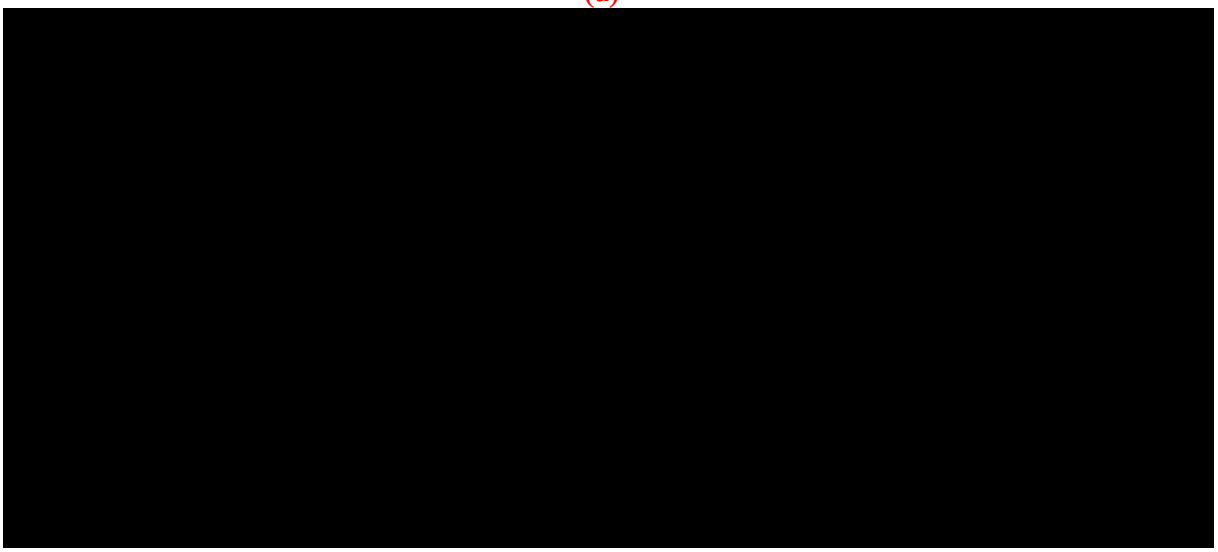

(b)

Figure 5.33: (a) The estimated and measured rotor angle (experimental results), (b) The estimation error (experimental results).

The error of the position in Figures 5.32 (b) and 5.33 (b), are mostly due to the natural delay of the observer and the filters. It can be seen more clearly at the moments when the angle jumps E H W Z H H Q µ ¶ D Q G µ Œ ¶ $ W W K H V H spikes. At zero speed, when there U U R U D is no jumping, the spikes cannot be seen. Figures 5.34 (a) and 5.35 (a) also show the estimated

(a)

(b)

The simulation and experimental results for vector control are presented in this section. The simulation and experiment run for 20 seconds and the load is a damping load according to equation (5.164). The speed reference is a trapezoidal one that starts from zero and covers positive and negative rotor speeds.

$$T_L \quad 0.01\,\omega_r \tag{5.164}$$

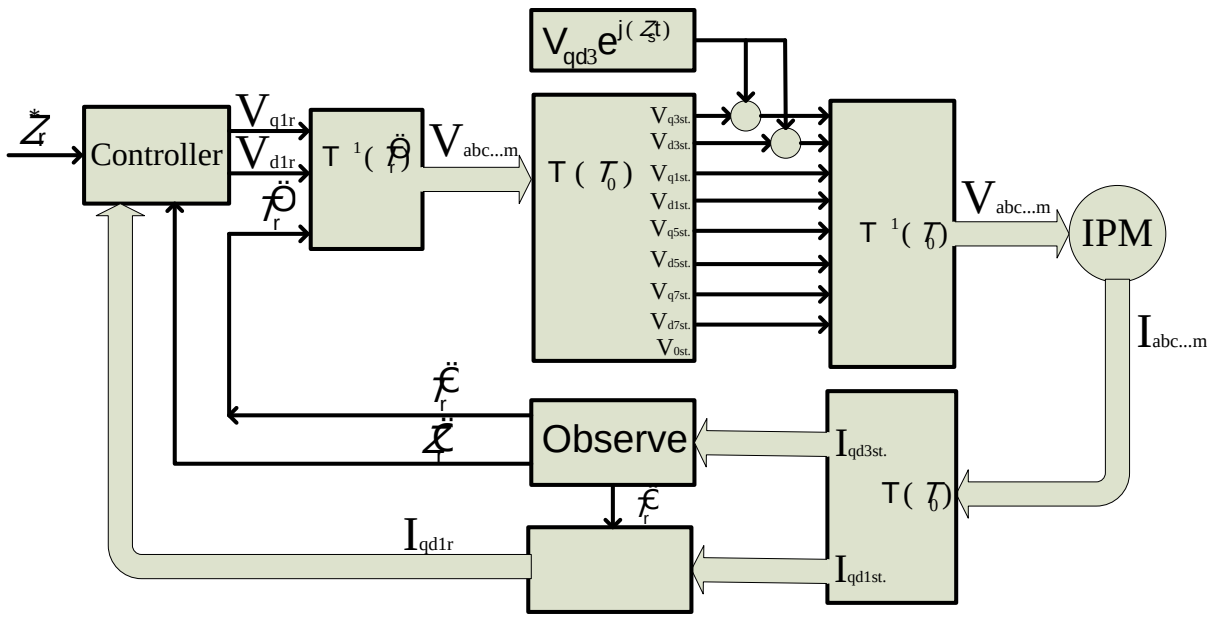

Figure 5.36: The controller of the IPM machine with observer.

The following figures show the drive results. The rotor speeds for simulation and experiment are shown in Figures 5.37 and 5.38 respectively. Figure 5.37 (a) shows the reference speed and the gure.4(the q662)( )( )9(a4(r r)4(l.16)3(4).)9(rotor rotor)4.)9(r139(re)7(re)7(99(ve.16)4(e)3)-129l

(a)

(b)

Figure 5.38: (a) Reference and rotor speed (experimental results), (b) The speed error (experimental results).

Figure 5.39 show the simulation result of the q axis voltage in rotor reference frame. The experimental result of the same voltage is also shown in Figure 5.40. It can be seen that by increasing the rotor speed, when the load torque and consequently q axis current increases, the q axis voltage also increases to let the machine supply the load. Figures and 5.41 and 5.42 show the

output voltages of the controller loops for d axis in rotor reference frame for simulation and experimental results respectively. The q and d axis voltages are transformed to real quantities and the resulting nine phase voltages are used to generate appropriate nine-phase PWM signals.

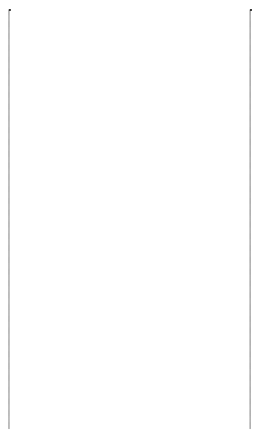

Figure 5.39: The q axis voltage in the rotor reference frame (simulation result).

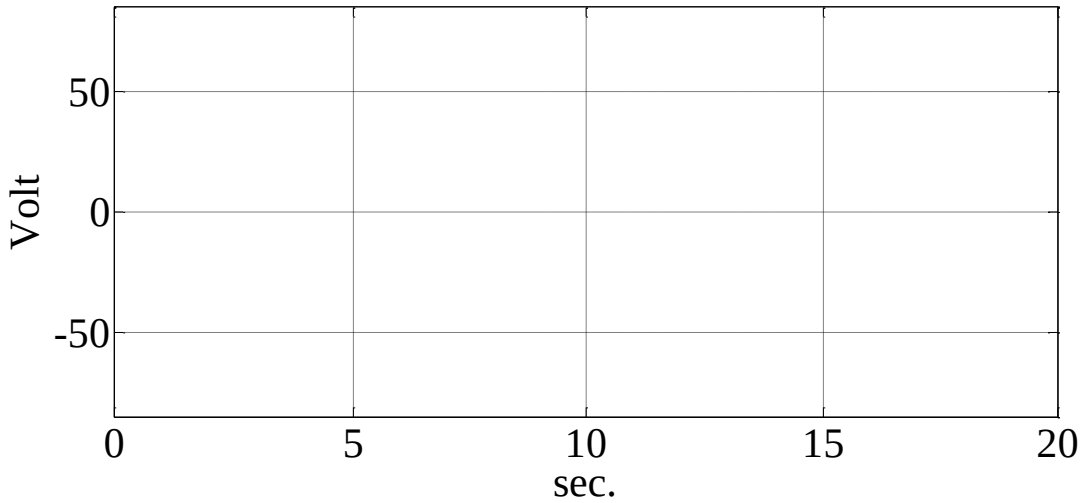

Figure 5.40: The q axis voltage in the rotor reference frame (experimental result).

Figure 5.41: The d axis voltage in the rotor reference frame (simulation result).

Figure 5.42: The d axis voltage in the rotor reference frame (experimental result).

The reference and simulated current of the d axis in rotor reference frame are shown in the Figure 5.43. The reference current is generated from the q axis current according to minimum copper loss strategy. It can be seen that the machine current tracks the reference. The reference and

(a)

(b)

Figure 5.43: (a) The d axis currents, reference and actual (simulation results), (b) The current controller error (simulation results).

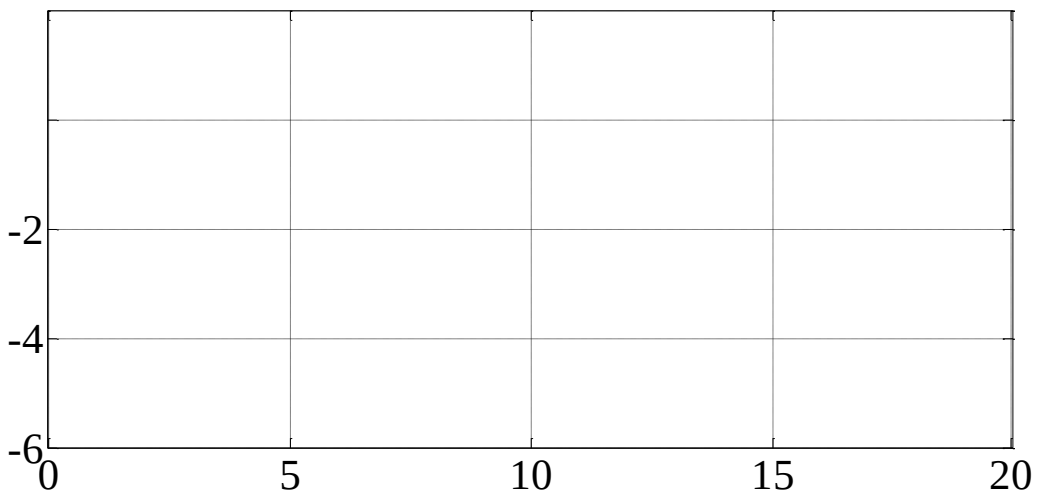

(a)

(b)

Figure 5.44: (a) Reference and actual currents for the d axis in the rotor reference frame (experimental results), (b) The error between the reference and feedback currents (experimental results).

The reference and simulated current of the q axis in rotor reference frame are also shown in the Figure 5.45. The reference current is generated from the speed control loop and it is clear that the machine current tracks the reference.

(a)

(b)

(a)

(b)

Figure

(a)

(b)

(c)

Figure 5.50: The nine- S K D V H F X U U H Q W V R I W K H P D F K L Q H I R U

D Q G µ K ¶ F µ F ¶ µ I ¶ D Q G µ L ¶ U R W R U results (F A/scale).X

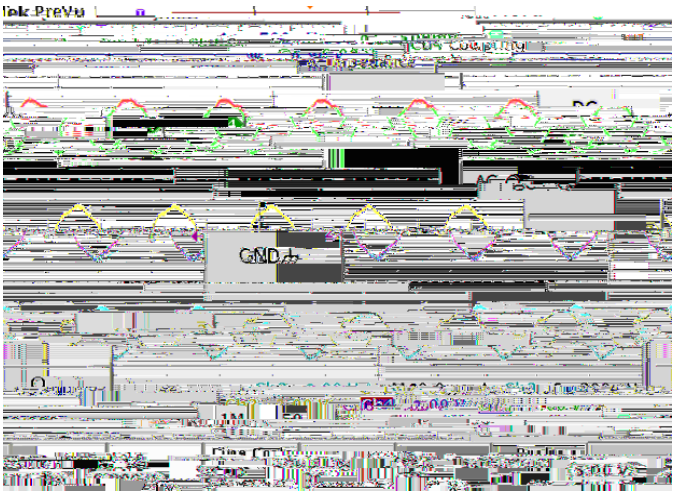

(a)

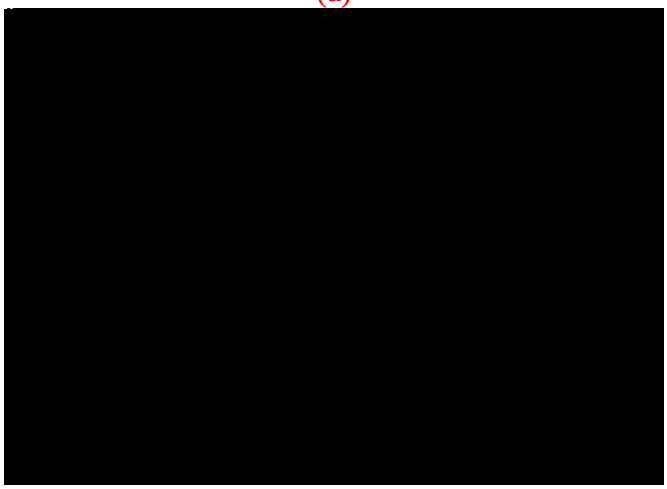

(b)

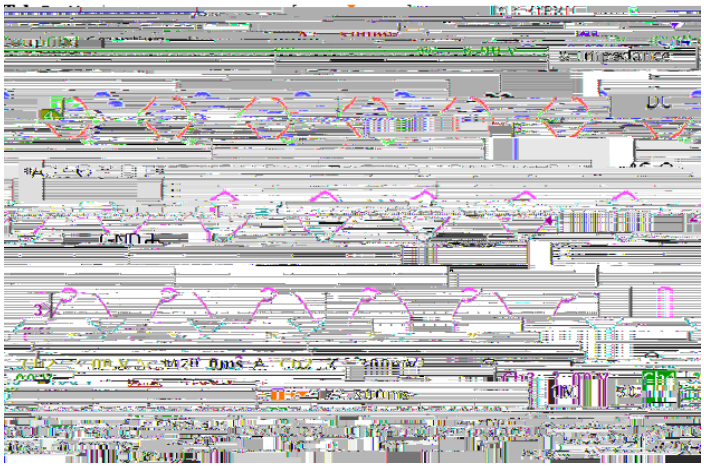

(c)

Figure 5.51: The nine- S K D V H F X UÉ Xà(c)

(a)

(b)

Figure 5.52: (a) The dq_3 currents before heterodyning (simulation results), (b) The dq_3

The third sequence of the nine-phase currents need to be extracted to be used for position

(a)

(b)

Figure 5.55: (a) The dq_3 currents after heterodyning 461 g 6C.45 gsT/F1 12.ETQ 72.024 2u9q7Te0 0 r8s

To extract the low frequency component, the generated signals are multiplied to term A? Ý ÞÇ the result signals are shown in the Figure 5.54 and 5.55 for simulation and experimental results respectively. It can be seen that the currents have a low frequency part which can be extracted using a low pass filter.

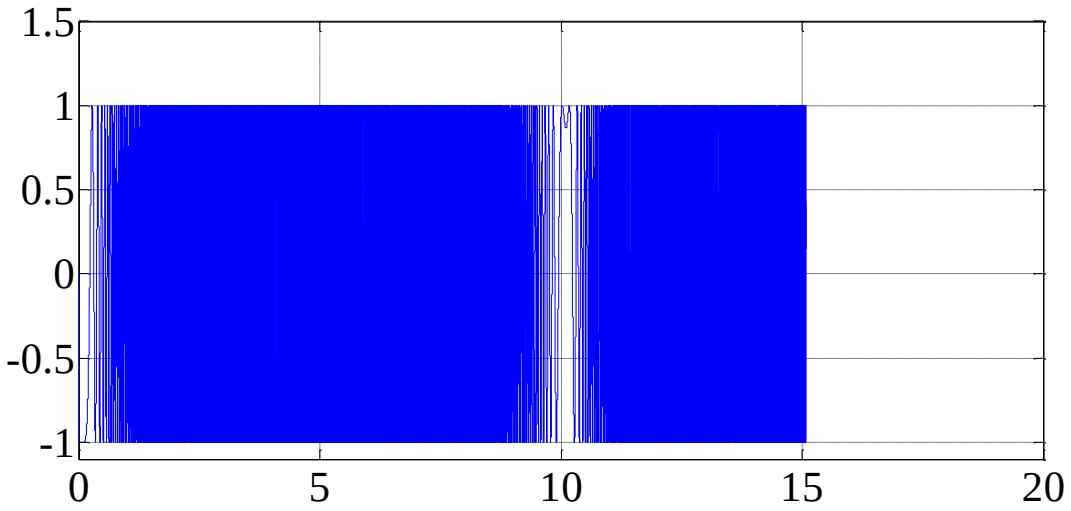

Figure 5.58: The normalized currents fed to observer. (simulation results).

Figure 5.59: The normalized currents fed to observer. (experimental results).

From Figures 5.58 and 5.59, it can be seen that the magnitudes of the currents are fixed to unity. Now the currents are suitable to be fed to the Lunberger observer that was designed in pervious sections. The currents are fed to the Lunberger observer to estimate the rotor angle.

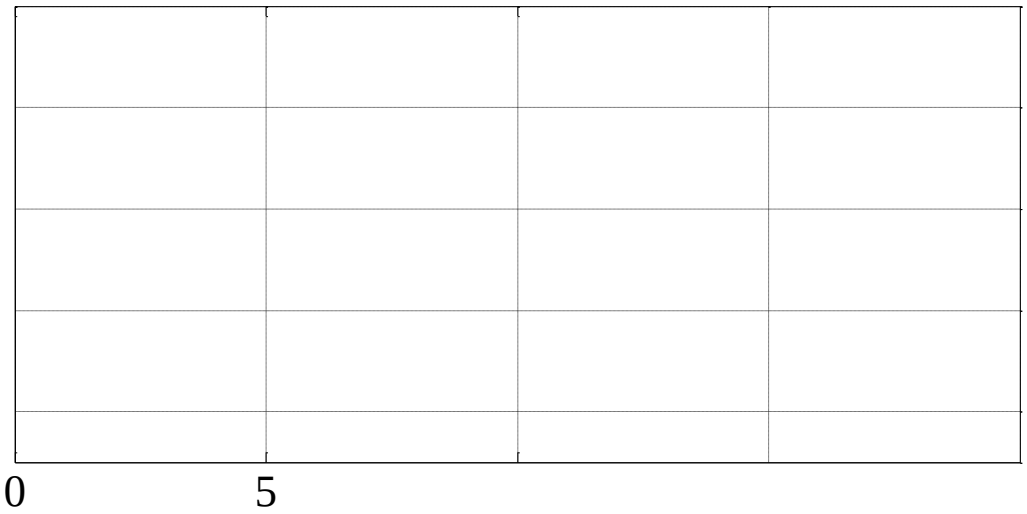

(a)

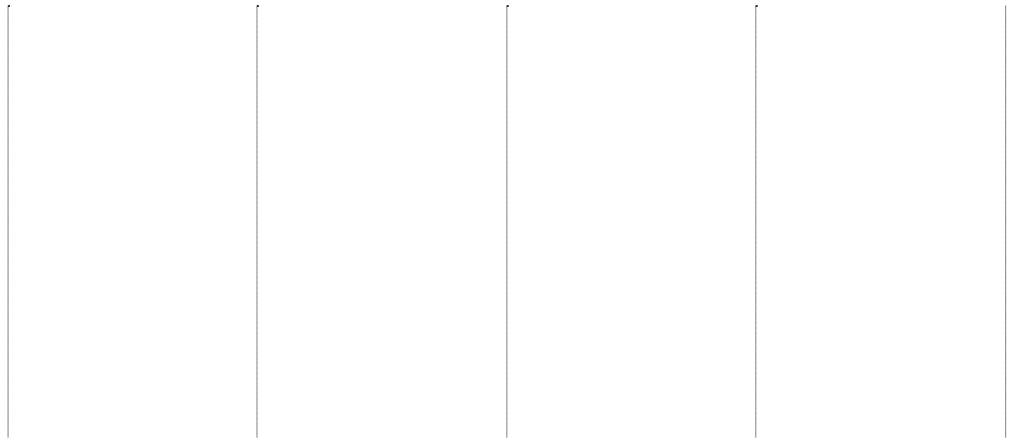

(b)

Figure 5.60: (a) Estimated and simulated rotor angle (simulation results), (b) Estimation error (simulation results).

Figures 5.60 and 5.61 show the estimated and rotor angle for simulation and experiment along with the estimation error.

(a)

(b)

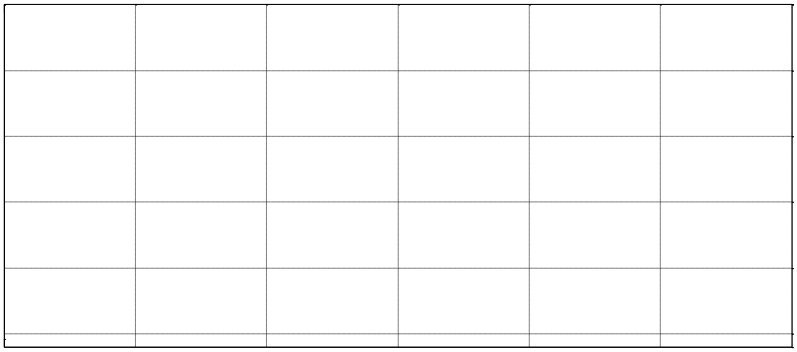

(a)

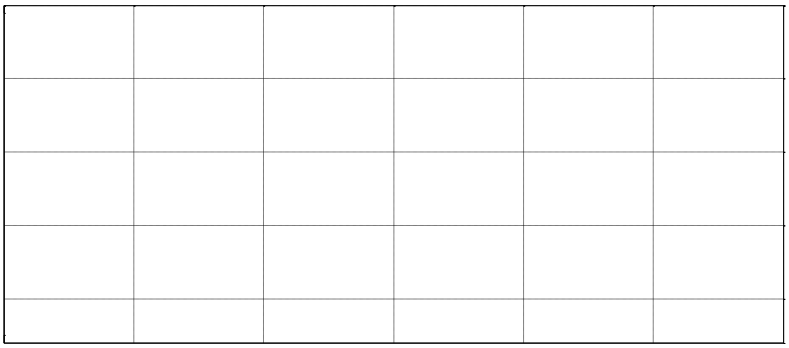

(b)

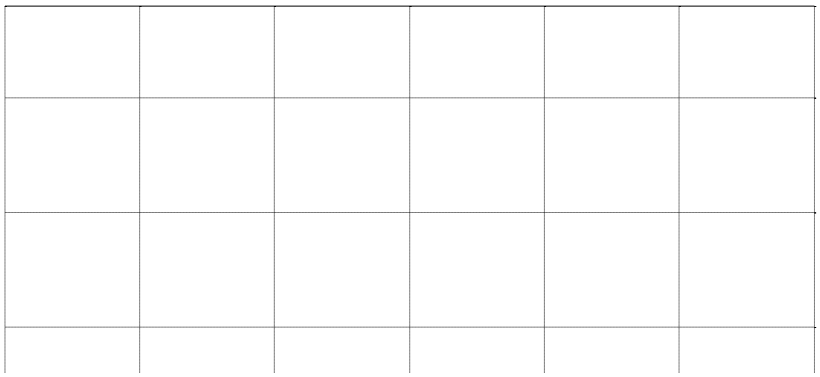

(c)

Figure 5.63: (a) The normalized currents fed to observer around rotor speed zero crossing (experimental results), (b) Estimated and measured rotor angle (experimental results), (c) The estimation error (experimental results).

(a)

(b)

Figure 5.65: (a) The reference and rotor speed (experimental results), (b) Speed error (experimental results).

Figures 5.64 and 5.65 show the reference speed and the rotor speed together along with the

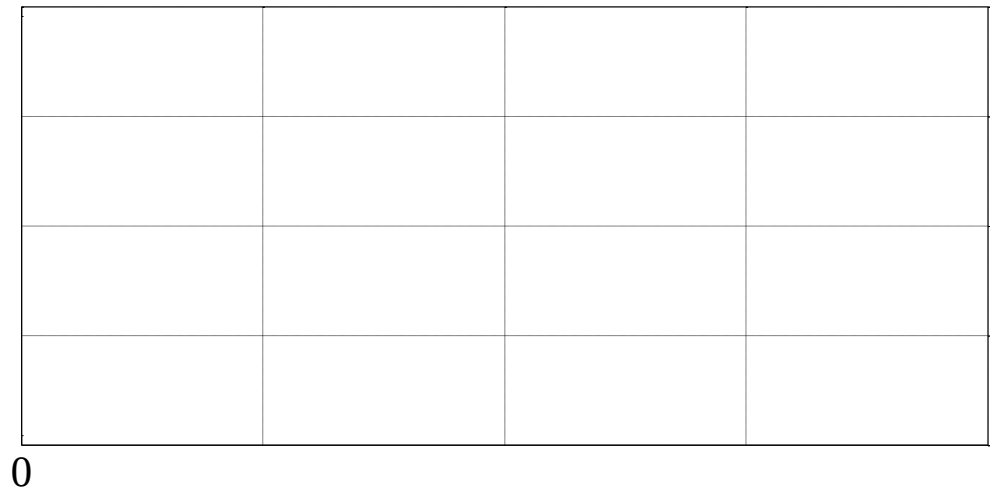

Figure 5.66: The electromagnetic torque of the machine (simulation results).

Figure 5.67: The electromagnetic torque of the machine (experimental results).

The Figure 5.64 (b) and 5.65 (b) show the speed error for simulation and experiment respectively. Figures 5.66 shows the electromagnetic torque of machine and the load torque for simulation and 5.67 shows the electromagnetic torque of machine for experiment. From both figures it can be seen that, by applying the load, machine generated electromagnetic torque to keep the rotor speed constant.

Figure 5.70: The voltage generated by the current regulators d axis of the rotor reference frame (simulation results).

axis current and consequently d axis current, the d axis voltage increases in negative side to let the essential d axis current flow to the machine stator.

Figure 5.72: The q axis reference and feedback currents (simulation results).

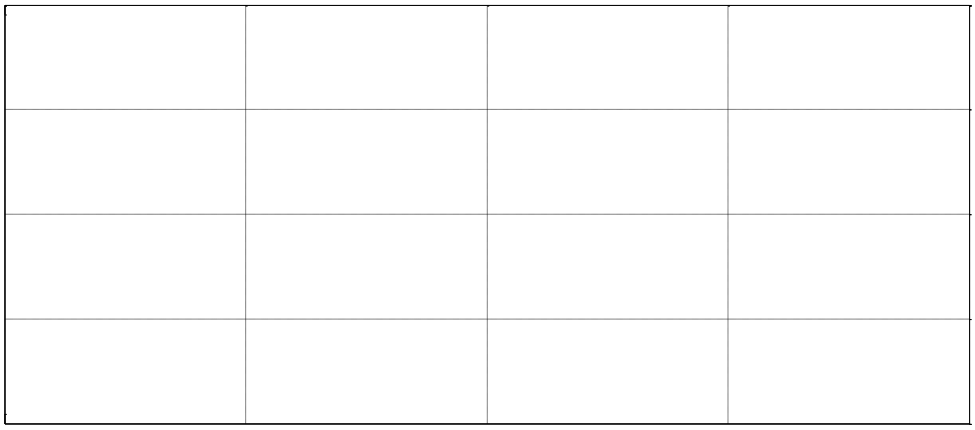

Figure 5.73: The q axis reference and feedback currents (experimental results).

Figures 5.72 and 5.73 show the reference and measured currents in q axis of the rotor reference frame for simulation and experimental respectively. The q axis current is generated from

the speed error and it can be seen that, the q axis current increases when the load torque is applied to the machine shaft.

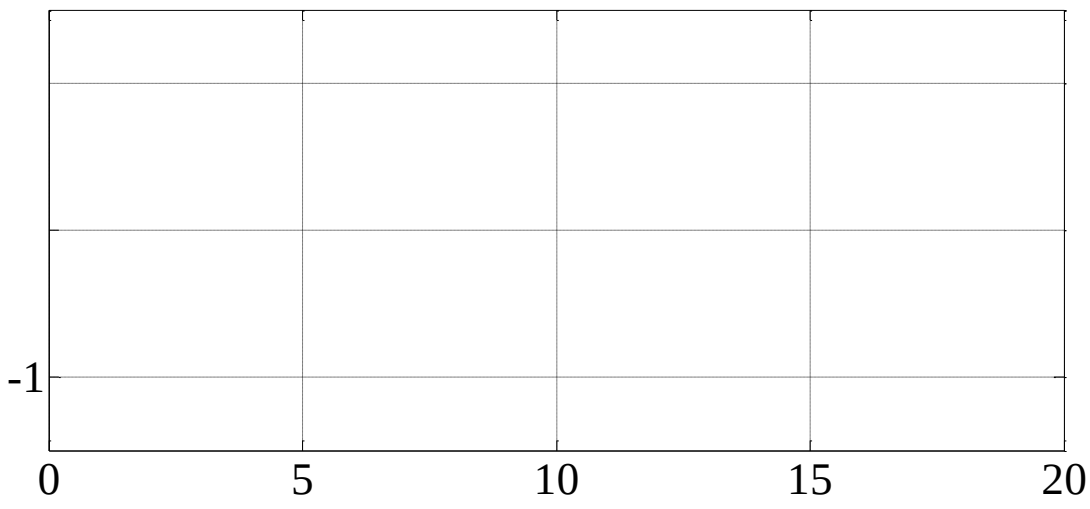

Figure 5.74: The d axis reference and feedback currents (simulation results).

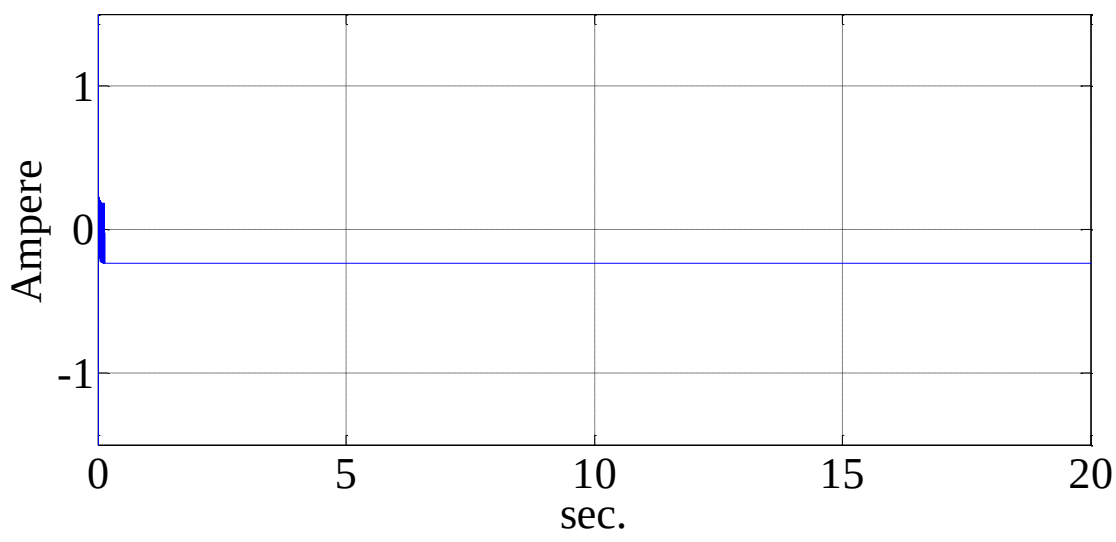

Figure 5.75: The d axis reference and feedback currents (experimental results).

Figures 5.74 and 5.75 show the reference and the feedback values for the d axis current for simulation and experiment respectively. The reference is again generated from the q axis current using the minimum copper loss strategy.

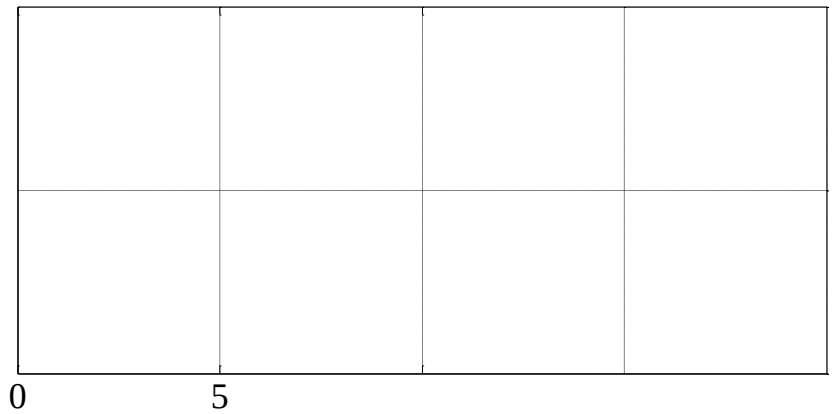

(a)

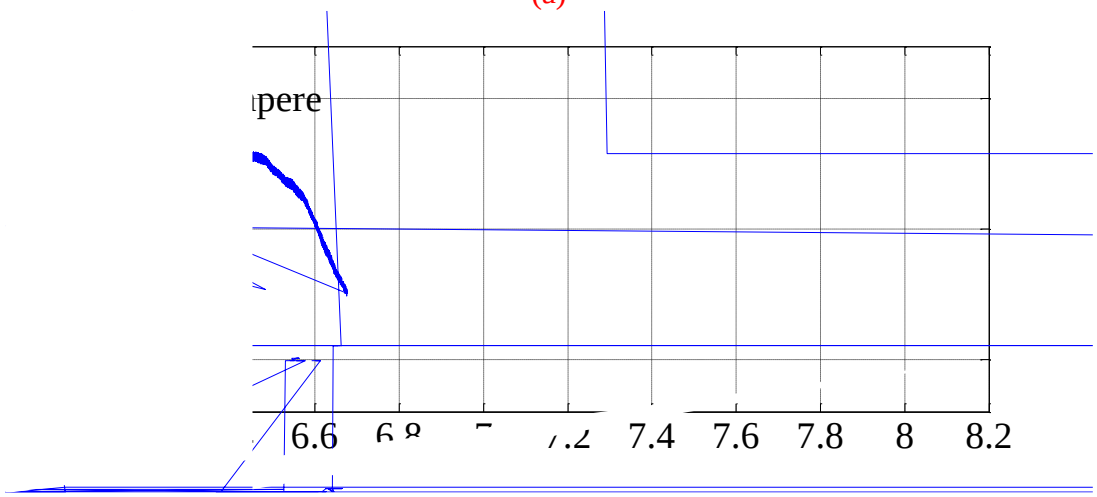

(b)

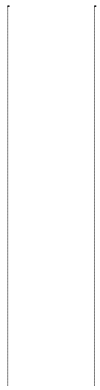

(c)

Figure 5.76: (a) The currents of the machine in natural variables (simulation results), (b) and (c) Zoomed view before and after load application respectively (simulation results).

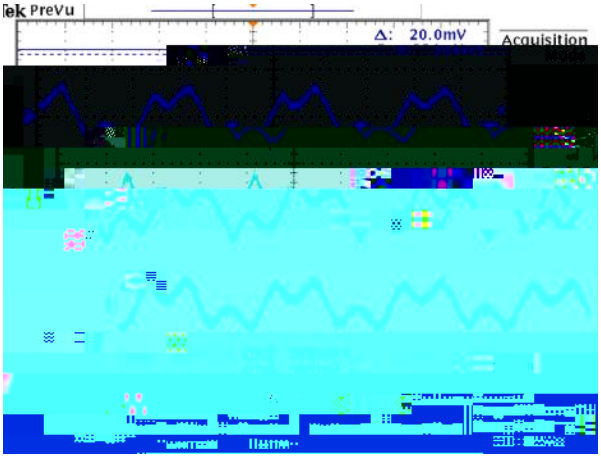

(a)

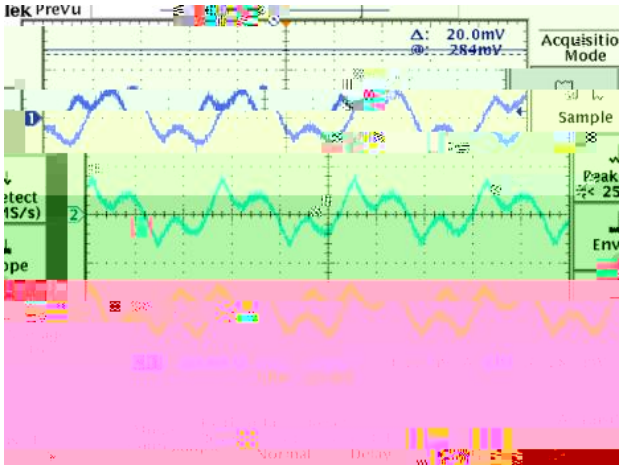

(b)

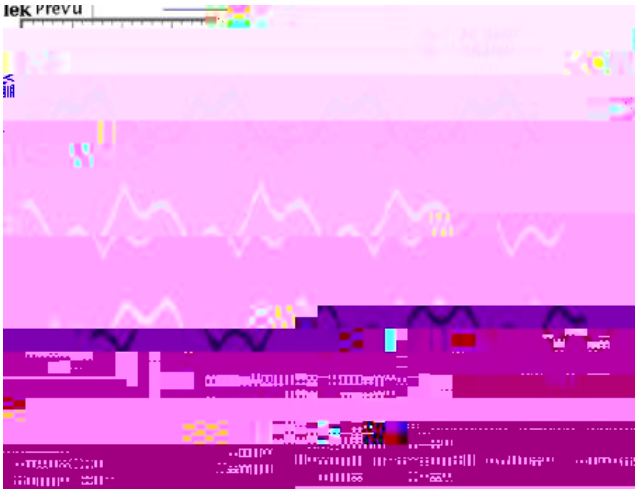

(c)

Figure 5.77: The nine-phase currents of the machine phases before applying load for phases,

D µ D ¶ µ G ¶ D Q G µ J ¶ E µ E ¶ µ H ¶ D Q G µ K ¶ scale). µ F

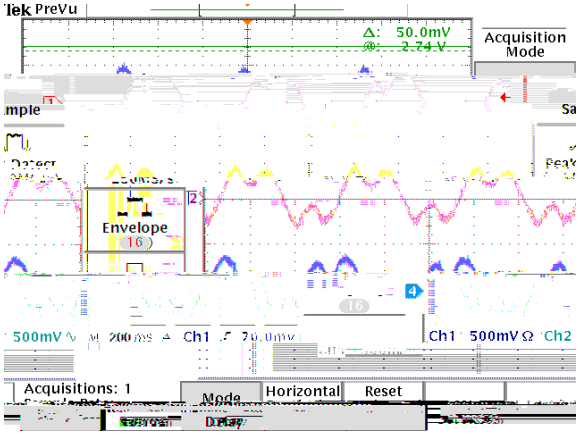

(a)

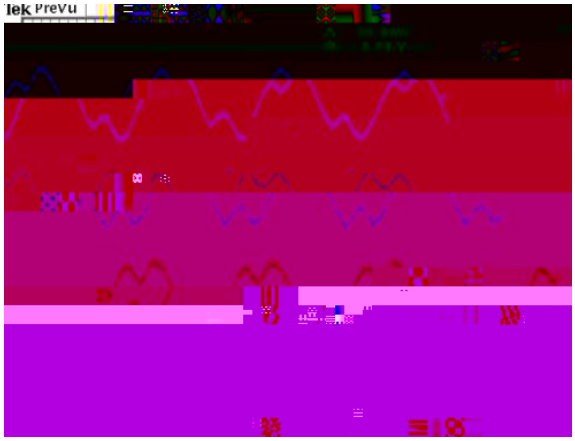

(b)

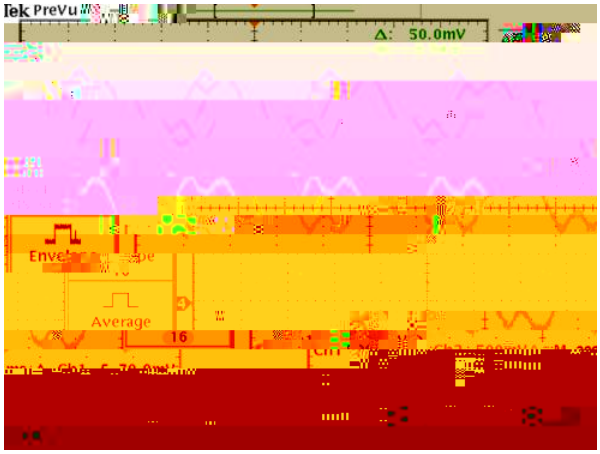

(c)

Figure 5.78: The nine-phase currents of the machine phases after applying load for phases for S K D V H V D µ D ¶ µ G ¶ D Q G µ J ¶ E µ E ¶ µ H ¶ D Q G µ scale).

(a)

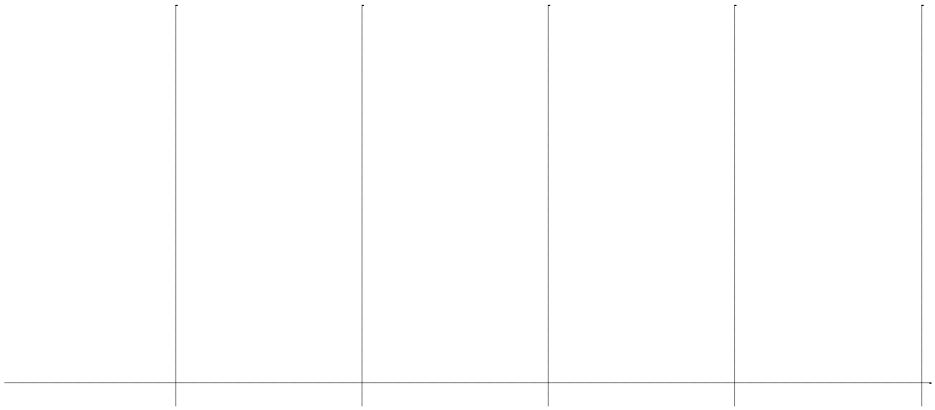

(b)

Figure 5.79: (a) The third sequence of the stator current in the stationary reference frame (simulation results), (b) The zoomed view (simulation results).

Figure 5. 76 shows the simulation results of the stator currents. The effect of the increase in q and d axis current of the rotor reference frame can be seen from their peak magnitude. The stator currents of experimental results are also shown in Figures 5.77 and 5.78. Figure 5.77 shows the currents before applying load torque and Figure 5.78 shows the stator currents after applying load torque. There are some ripples on the currents of the experimental results which are due to the magnetic saturation of the machine stator and measurement noise.

(a)

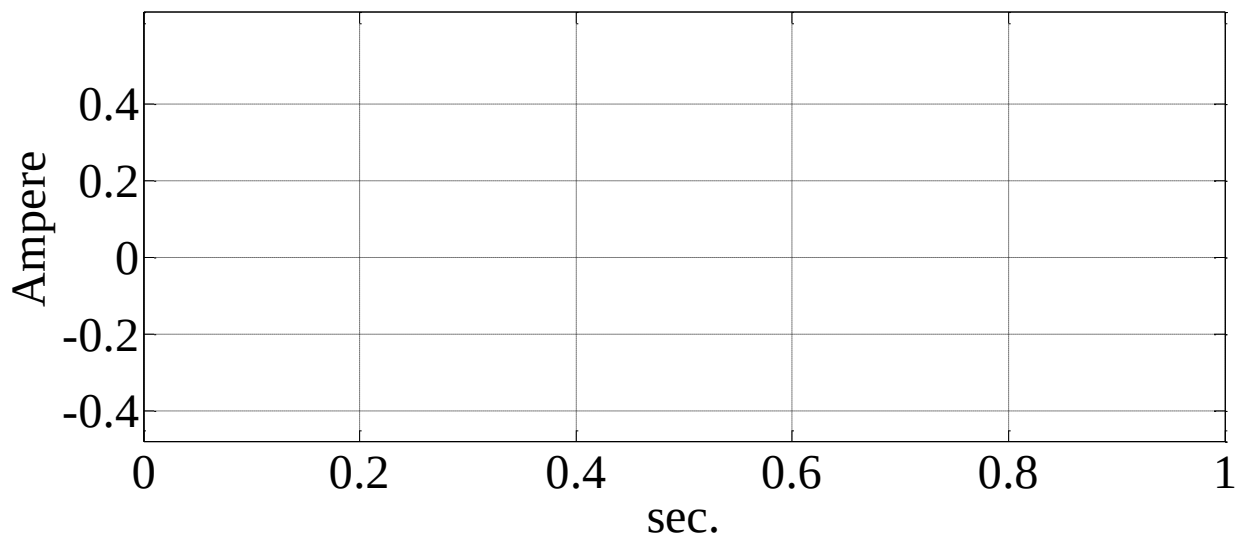

(b)

Figure 5.80: (a) The third sequence of the stator current in the stationary reference frame (experimental results), (b) The zoomed view (experimental results).

The third sequence currents of the stator are extracted and used for positon estimation. The Simulation and experimental results of the third sequence currents are shown in Figures 5.79 and 5.80 respectively. The currents in Figures 5.81 and 5.82 pass through a heterodyning block then

(a)

The signals of Figures 5.81 and 5.82 need to be normalized to have unity magnitude and be fed to the observer. Figures 5.83 and 5.84 show the signals after normalizing for simulation and experimental results respectively.

Figure 5.83: The normalized currents of the third sequence (simulation results).

The signals of Figure 5.83 and 5.84 carry the rotor position information. The rotor position now can be extracted using Luenberger observer. The signals are fed to the observer and the results are shown in Figures 5.85 and 5.86 for simulation and experiment respectively. These two figures show the rotor angle and the estimated one along with the estimation error.

(a)

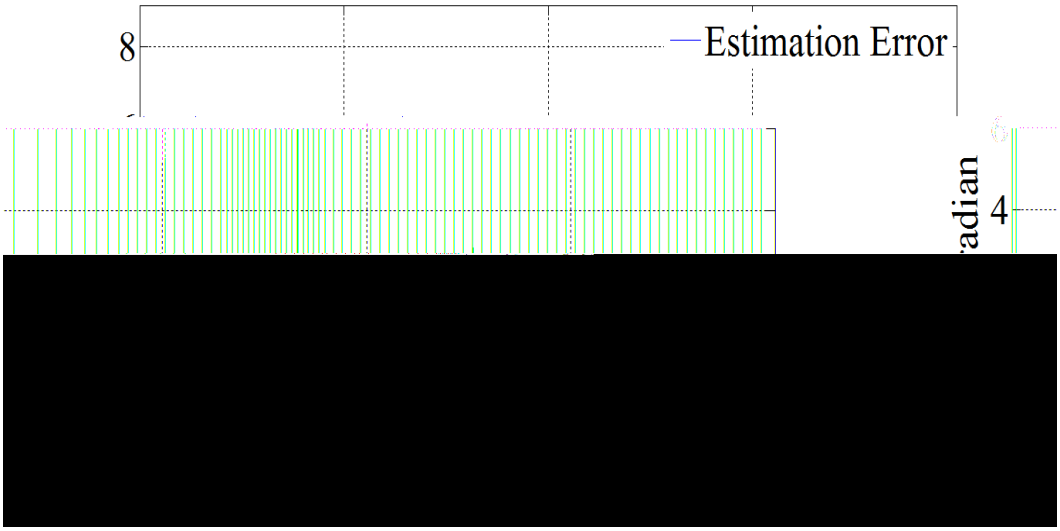

(a)

(b)

Figure 5.86: (a) The simulated and estimated angle (experimental results), (b) The estimation error (experimental results).

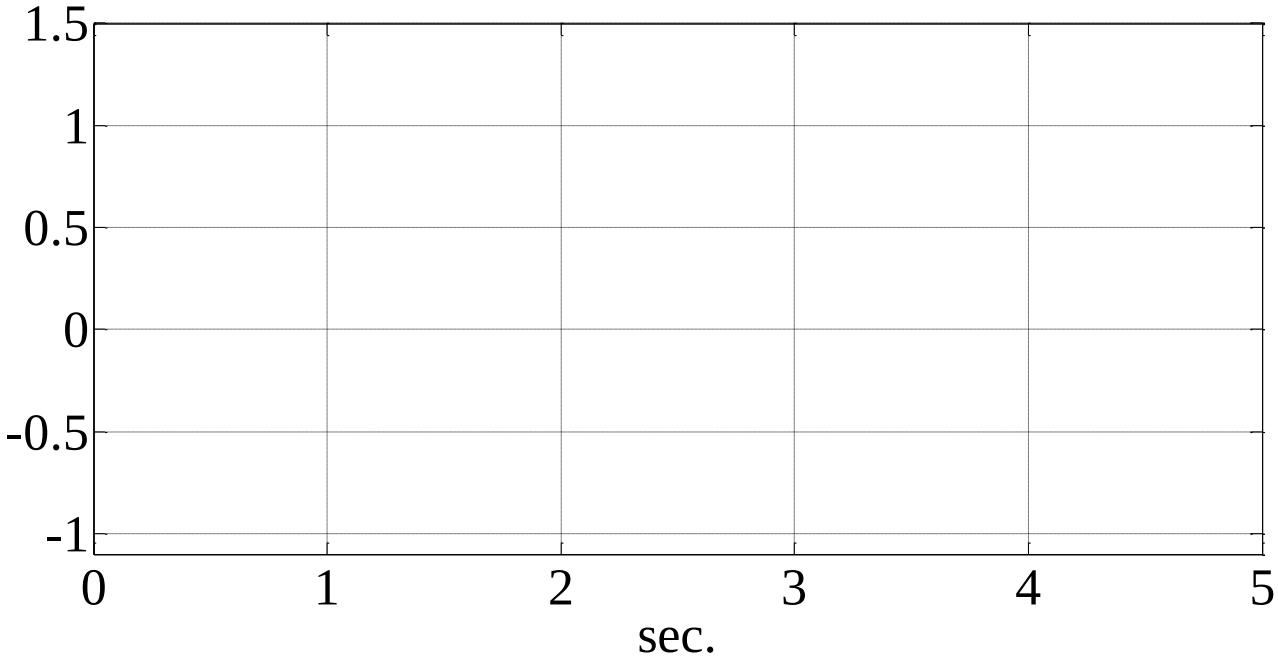

(a)

(b)

Figure 5.87: (a) The normalized currents of the third sequence (simulation results), (b) The simulated and estimated rotor angle at the starting interval (simulation results).

(a)

(b)

5.6.4 Very Low Speed Run

The last test is the same controller in a very low speed. In this test the machine runs at the speed of 0.3 rad/sec and a step load is applied to the machine when it is in the steady state. The following figures show the simulation and experimental results. The speed reference starts from the zero and goes to a fixed speed at 0.3 (rad/sec) after drive settles down to the steady state conditions a step load torque is applied to the rotor for 10 seconds.

(a)

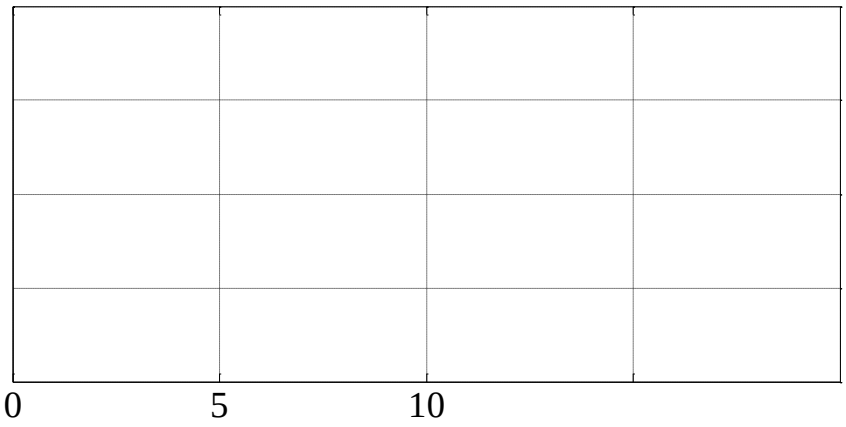

(b)

Figure 5.89: (a) The rotor speed and the reference speed (simulation results), (b) The speed error (simulation results).

(a)

(b)

Figure 5.90: (a) The reference and rotor speed (experimental results), (b) The speed error (experimental results).

Figures 5.89 (a) and 5.90 (a) show the reference and rotor speed for simulation and experimental results respectively. From these figures, it can be seen that the drive can track the rotor reference accurately. For b/F1

that, the drive can react to the load torque and generate proper electromagnetic torque to keep the rotor speed constant.

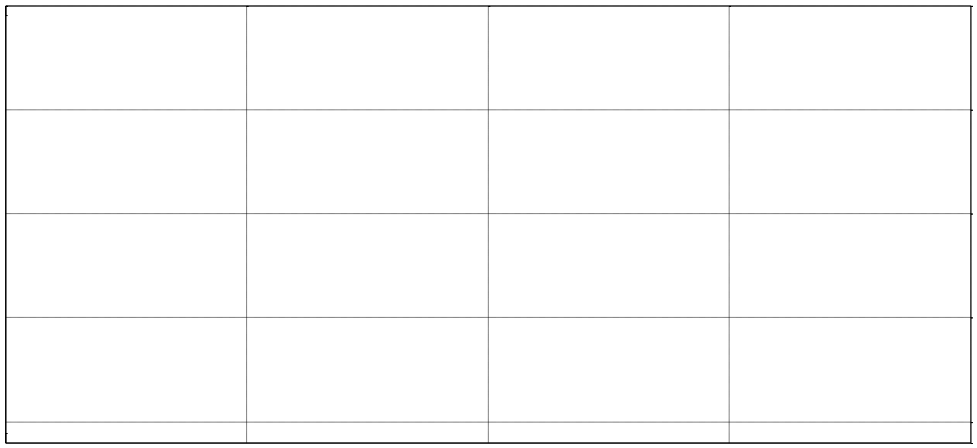

Figure 5.91: The load and electromagnetic torque (simulation results).

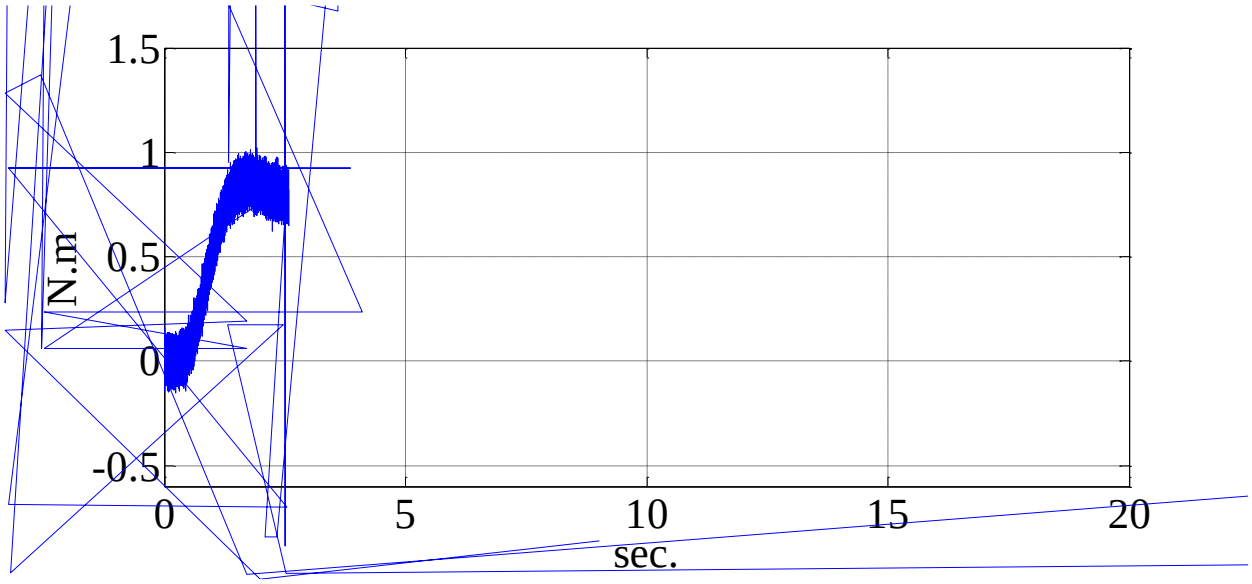

Figure 5.92: The electromagnetic torque of the machine (experimental results).

The voltages generated by machine controller in rotor reference frame are shown in the Figures 5.93 and 5.94 for simulation and experimental results respectively. Again from this Figures the reaction of the drive to the changes of the load on the motor shaft can be seen.

Figure 5.94: The q and d axis voltage of the machines in the rotor reference frame generated by the controller (experimental results).

The generated voltages are applied to the machine to inject the desired currents to the stator. Figures 5.95 and 5.96 show the reference and measured current of q axis

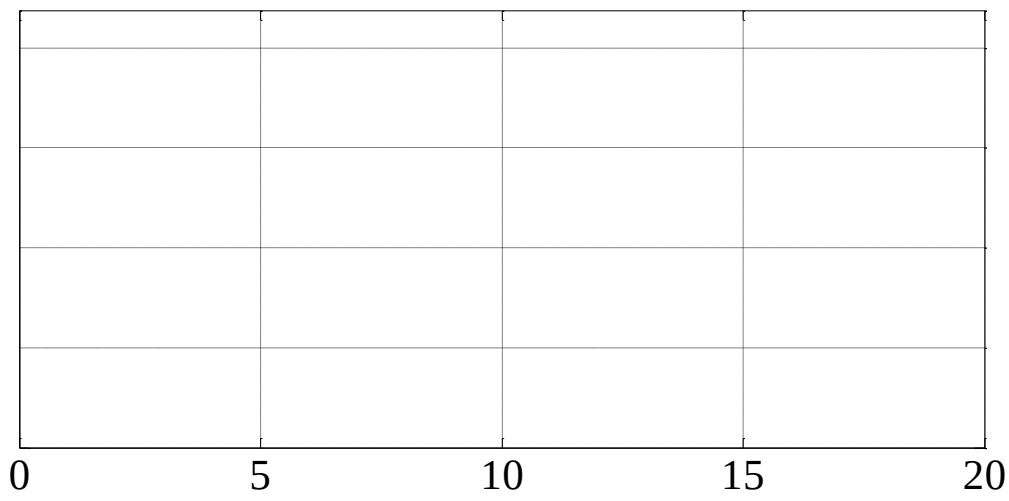

(a)

Figure 5.95: The reference and the feedback currents in rotor reference frame for q axis (simulation results).

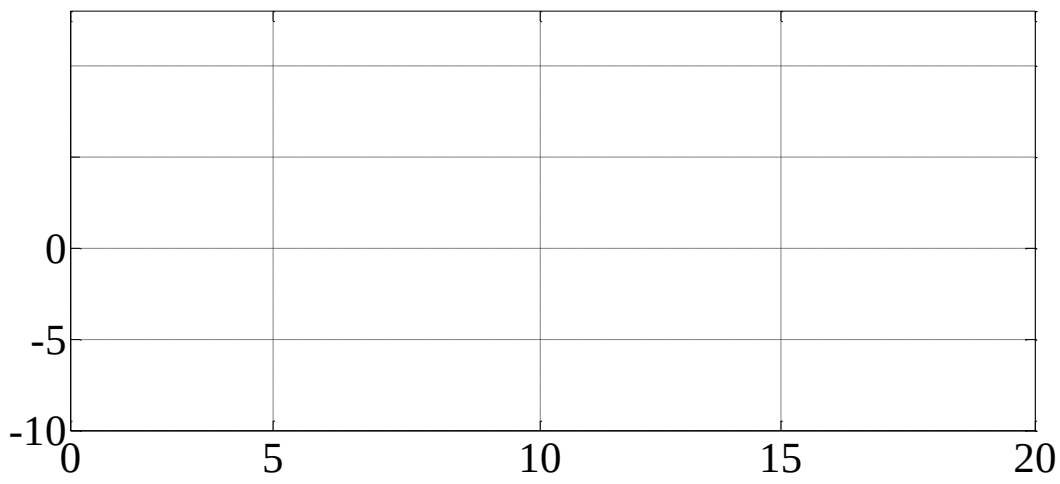

Figure 5.96: The reference and the feedback currents in rotor reference frame for q axis (experimental results).

Figures 5.97 and 5.98 also show the reference and measured current of d axis reference frame for simulation and experiment respectively.

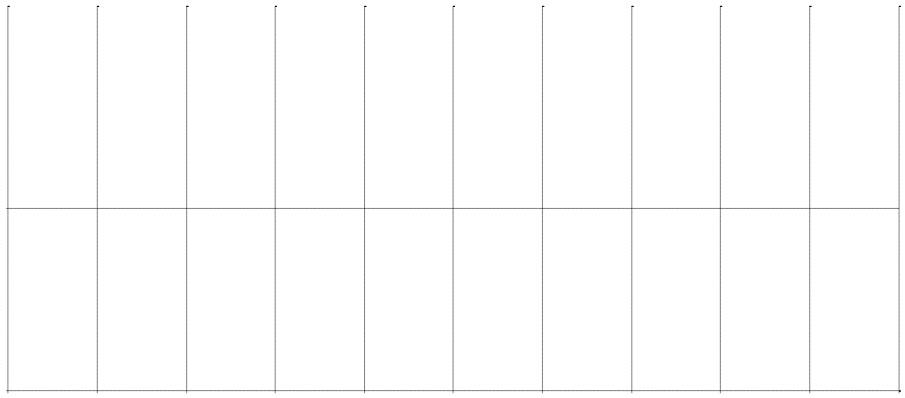

(a)

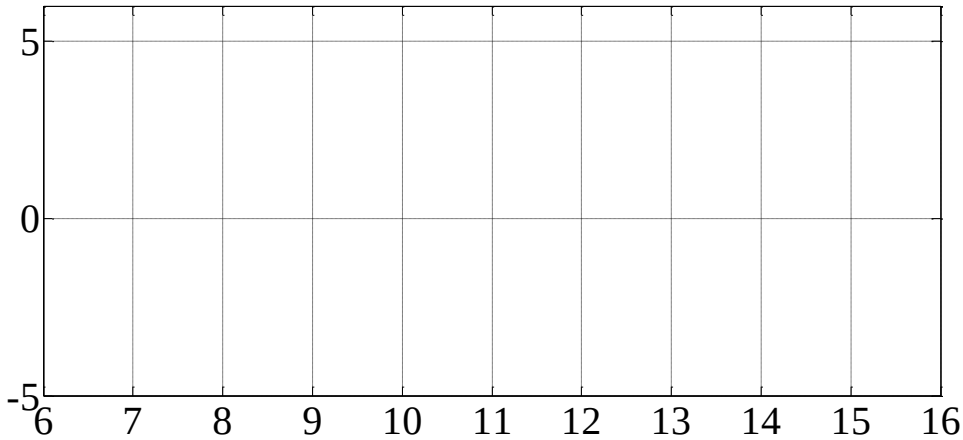

(b)

Figure 5.99: The simulation result of nine-phase stator currents, (a) Before applying load torque, (b) After applying load torque.

The currents of the third sequence of stationary reference frame are shown in the Figure 5.102 and 5.103 for simulation and experiment respectively. These currents are derived from the { H { transfer matrix in stationary reference frame. These currents can be used for signal processing and position estimation process. From these figures, it can be seen that, the third sequence currents have variable magnitudes. The ripples on the magnitudes are caused by the rotor saliency and they can be used for position estimation.

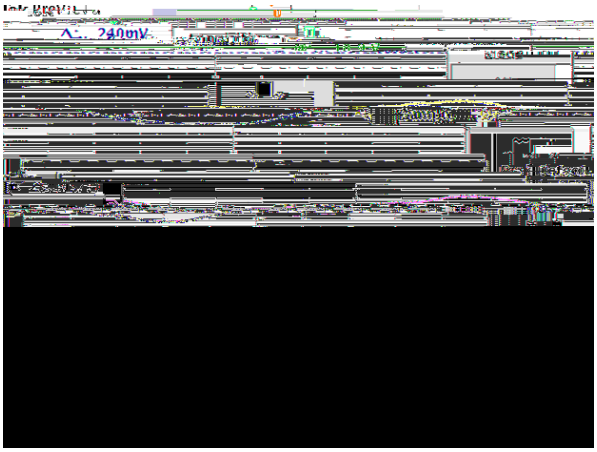

(a)

(b)

(c)

Figure 5.100: The nine-phase currents of the machine phases before applying load for phases, (a) µ D ¶ µ G ¶ D Q G µ J ¶ E µ E ¶ µ H ¶ D Q G results ¶ (5 A/F scale) µ F ¶

(a)

(b)

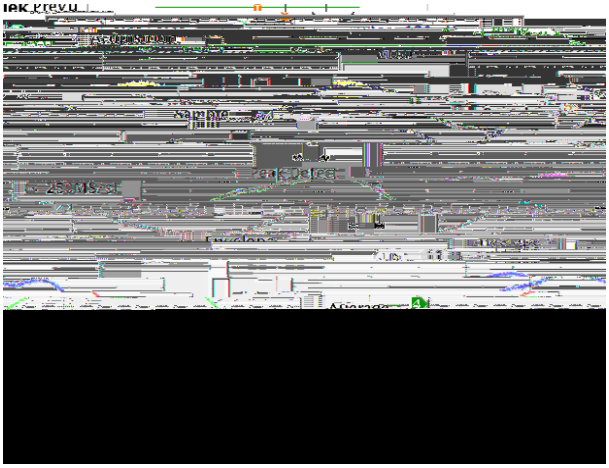

(c)

Figure 5.101: The nine-phase currents of the machine phases after applying load for phases for phases,

D µ D ¶ µ G ¶ D Q G µ J ¶ E µDEQ¶G µµ HL ¶ DHQ[G HµUKL¶P HsQ[¶ µDFO¶

Figure 5.102: The dq_3 currents before heterodyning (simulation result).

Figure 5.103: The dq_3 currents before heterodyning (experimental result).

Again since the currents after filtering have variable magnitudes which vary with the rotor speed they need to be

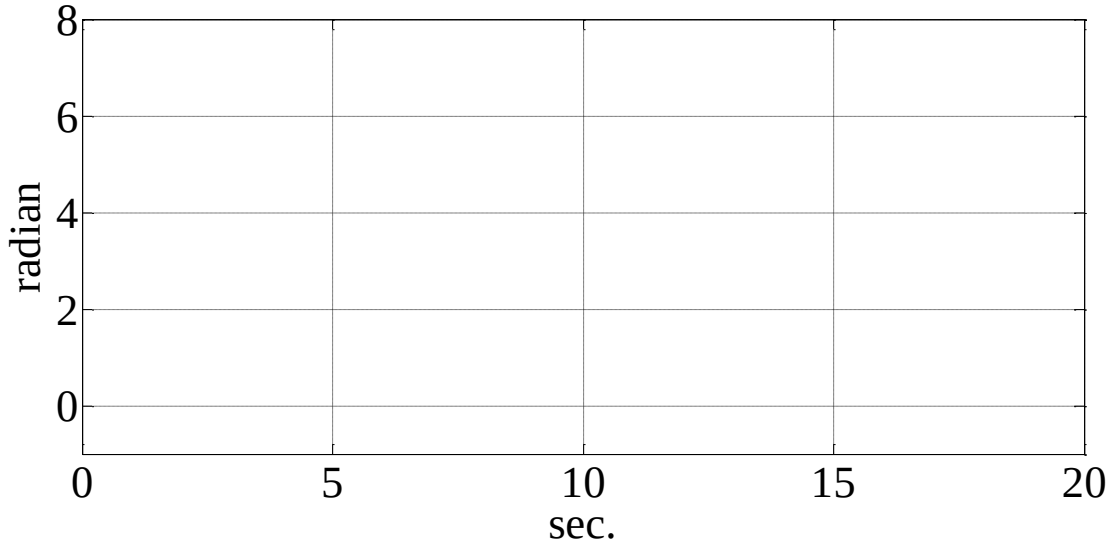

(a)

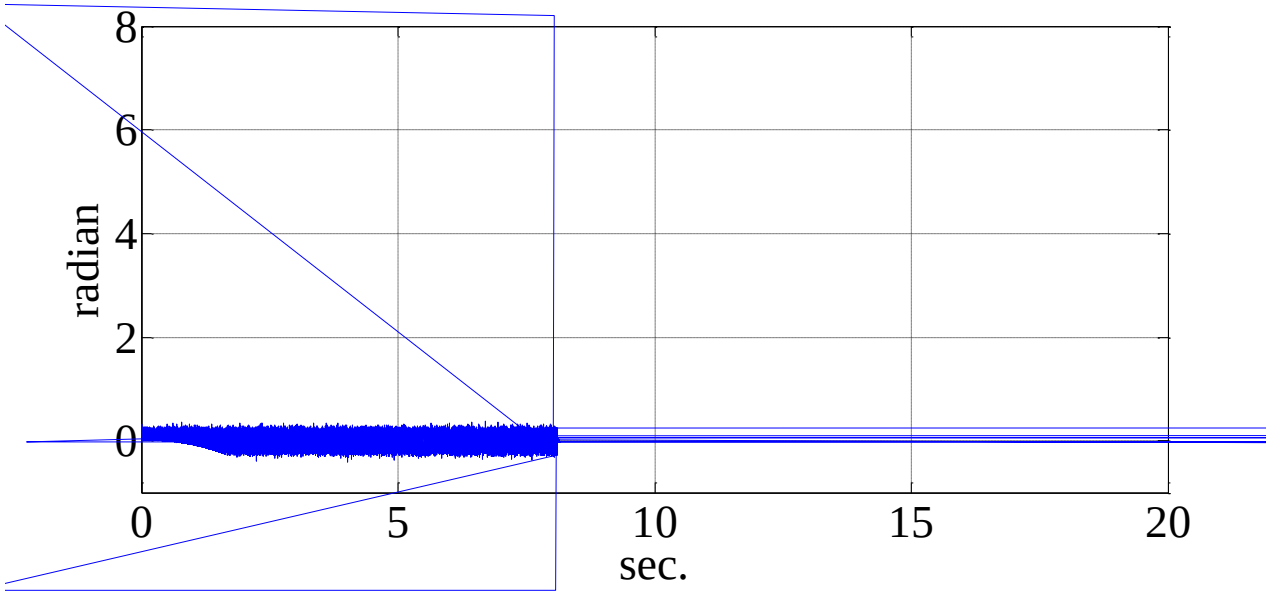

(b)

Figure 5.109: (a) Estimated and measured rotor angle (experimental results), (b) The estimation error (experimental results).

Figure 5.112: The stator phase voltage.

Figure 5.113: The copper loss of the machine.

sections of this chapter the steady state performance of the machine is analyzed using FEMM for different stator current levels and operation modes of the controller.